University of Stavanger

Faculty of Science and Technology

MASTER'S THESIS

Study program/Specialization: Environmental Technology/ Offshore Environmental Engineering	Spring semester, 2014 Open
Writer: Susann Aloysius Haug	(Writer's signature)
Faculty supervisor: Merete Vadla Madland	
Title of thesis: The chemo-mechanical effects of carbonated water at realistic reservoir conditions	
Credits (ECTS): 30	
Keywords: • Kansas chalk • Carbonated sea water • CO_2 storage • EOR • Water weakening • Chemical alteration	Pages: 107 +enclosure: N/A Stavanger, 10.03.2014

Front page for master thesis

Faculty of Science and

Technology

The chemo-mechanical effects of carbonated water at realistic reservoir conditions

by

Susann Aloysius Haug, BSc

Thesis

Presented to the Faculty of Science and Technology

The University of Stavanger

The University of Stavanger

March 2014

Dedication

To my boys, Adrian & André.

My biggest motivation

Acknowledgements

With this I would like to express my deepest gratitude towards *Dr. Anders Nermoen* for his excellent supervision during my master project. With your enthusiasm, positive attitude and professional skills you have guided me through this project every step of the way. I have learned so much from working with you. Not only about rock mechanics, but also new ways of thinking and the joy of research. I have really enjoyed working with you.

My supervisor *Associated Professor Merete Vadla Madland*, thank you for giving me this opportunity and for letting me take part in your research team. There have been some challenging days, and I am forever grateful for your support. You are such an inspiring woman with your strength and determination combined with your kindness.

I would like to thank *Dr. Reidar I. Korsnes* for all help and for sharing his expertise. Thanks to Tania Hildebrand Habel for SEM-images.

I would also like to thank a very dear friend of mine, *Stine Finnesand*, for her technical support.

Special thanks go to my nearest friends and family, especially my mum and dad for all their help and support through this process.

Susann Aloysius Haug, Stavanger 08.03.14

Abstract

The possibility of CO_2 capture coupled with sequestration in deep geological formation has emerged in attempt to reduce the significant increase of $CO_{2\,(g)}$ in the atmosphere. The impact of CO_2 on the reservoir integrity should be extensively investigated in order to predict the long-term effects of CO_2 sequestration.

The solubility of chalk material is pH dependent. CO_2 dissolved in sea water will react to form carbonic acid. Subsequently, bicarbonate is formed and the acidity is increased. Our initial hypothesis was that "flooding of carbonated water weakens the chalk and additional strains are expected".
Three long-term flooding experiments performed on Kansas outcrop chalk has been analyzed in this thesis. All tests were performed at uni-axial strain conditions with some variations in test procedure for each experiment. We evaluate the sensitivity in the creep rate to the pore fluid composition, and we address the questions: Does the injection of sea water reduce the mechanical strength of compacted outcrop chalk at elevated stress and temperature? And to what degree will the injection of carbonated sea water further contribute to reduce the mechanical strength?

The results of our investigation were that the injection of carbonated water did not result in an increase of the creep strain rate in any of the three experiments during creep. The axial creep strain increased with 0.1, 0.4 and 0.5 % after the flooding with carbonated water was initiated which is not more than what was expected from the extrapolated creep curve before flooding. Based on our findings we conclude that under in-situ conditions CO_2 dissolved in sea water does not increase the creep strain rate, but provides a small chemical driven additional strain.

Table of Contents

List of Tables

List of Figures

1. INTRODUCTION

The similarities between reservoir chalk and outcrop chalk enables us to perform experimental testing on outcrop chalk in attempt to understand the physical and chemical processes of the reservoir rock.

The elastic case with linearity between stress state and observed strain defines elastic parameters. Thus, any change in stress impact reversible deformation. The elastic parameters of the material may be pore fluid dependent. Any weakening causes a reduction in these parameters.

The stress state at which the observed strain deviates from a linear trend is termed the onset of yield. The onset of yield is in our case also related to irreversible deformation where grain reorganization starts. The grain reorganization causes collapse of the pore space. Therefore, this yield phenomenon is termed pore collapse. Heterogeneity can possibly explain the observed range in which the stress-strain curve bends. As such, the yield may be better captured by the pragmatic yield. Any potential weakening is associated with a reduction in the onset of yield and pragmatic yield.

The observed deformation at constant stress conditions is termed creep. The strength concept is related to the rate of deformation; a weak material deforms at a higher rate than a stronger material. In this thesis, we evaluate the sensitivity in the creep rate to the pore fluid composition, and we address the questions: Does the injection of sea water reduce the mechanical strength of compacted outcrop chalk at elevated stress and temperature? And to what degree will the injection of carbonated sea water further contribute to reduce the mechanical strength?

Several mechanical and chemical processes may contribute to the observed strain. The relationship can be expressed through the following equation for strain partitioning where the pore collapse is represented as mechanical strain and dissolution/precipitation as chemical strain: $\varepsilon_{Total} = \varepsilon_{Mechanical} + \varepsilon_{Chemical}$

In the experiments of the thesis we measure the evolution in the external dimensions, i.e. total length, diameter and volume of the chalk. Chemical processes such as dissolution and precipitation are driven by the non-equilibria between the chalk and the injected brines. We keep track of the ion composition thought the experiment by ionic chromatography measurements and we use this information to estimate the dynamic evolution in the solid volume.

The tests presented in the thesis are long-term experiments. They have been running for 249, 203 and 109 days. The results from analyzing the data which have been collected through several months are presented.

2. THEORY AND BACKGROUNDS

2.1. The Importance of Enhanced Oil Recovery Research

The energy demand of the world is increasing due to both economic and population growth. Fulfilling the energy demand comes with great challenges. Not only do we need more energy, but also cleaner energy. One third of the world's energy consumption is accounted for by oil and natural gas accounts for 20 percent (2012). Norway is important in this context being ranked as the seventh largest oil exporter and the fourteenth largest oil producer in the world. As gas exporter Norway is the third largest and the sixth largest gas producer (2012). The petroleum sector is arbitrative in meeting the future energy demand, as long as there are no apparent energy sources that can account for the same output as oil and gas today. It is therefore important to utilize this resource optimally in the safest and most environmentally friendly way.

CO_2 enhanced oil recovery has been extensively investigated. Christensen, Stenby et al. (2001) published a review of the WAG (water alternating gas) field experience reported in the literature. The review consisted of about 60 fields, both onshore and offshore. Even though operational problems are often reported, there was a common successful trend with an increased oil recovery of 5-10% of the oil initially in place (OIIP). It is more beneficial in terms of the environment, cost and effectiveness to recover as much as possible from an existing reservoir than establishing new ones.

It is also stipulated in the Petroleum act paragraph §4-1 (1996) that "*Production of petroleum shall be conducted in such a way that most of the oil found in every single petroleum deposit, or in several deposits in combination, are produced. Production shall be in accordance with prudent technical and sound economic principles and so that waste of petroleum or reservoir energy is avoided."* The law understates the importance of conducting research and development within enhanced oil recovery (EOR) to ensure effective production with the goal of lower total release to the environment of chemicals and greenhouse gasses.

2.2. Water Weakening of Chalk

The Ekofisk field in the southern parts of the Norwegian North Sea is a well-known exampled when it comes to severe sea bed subsidence. Subsidence can be defined as the movement of surface stratum in response to loss of underground support (Nagel 2001). The Ekofisk field is an overpressured naturally fractured chalk reservoir that initiated production in 1971 (Sulak 1991). Subsidence of the sea bed was first observed in 1984, when the sea bed had subsided with approximately 3 m (Sylte, Thomas et al. 1999). This finding was unexpected because it was believed in that time that as long as the productivity was not declining, compaction would not occur. The sever compaction was explained by reduction in reservoir pressure when the reservoir was depleted. As the overlying layers continued to press down with the same weight, the chalk eventually gave in. Water injection was initiated in 1987 to maintain the pressure (Sulak 1991). The platforms on the Ekofisk field were jacked up by 6 meters, but the sea bed continued to subside and the Ekofisk field had to be developed all over again in. Production from Ekofisk II started in 1998 (Nagel 2001).

Several mechanisms have been suggested in attempt on explaining the compaction that still takes place after re-pressurization of the reservoir by water injection, the so-called “Water weakening effect” (Korsnes, Madland et al. 2008). Understanding the mechanisms behind the water weakening effect is crucial knowledge for oil companies in order to predict the behavior of the reservoir and to avoid the huge costs associated with sea bed subsidence. It is common to distinguish between pure mechanical effects, physico-chemical effects and pure chemical effects of the water weakening phenomenon.

The physical effects, in particular capillary forces which induce cohesion between chalk grains, have received great amount of attention through the years (Delage, Cui et al. 1996, Papamichos, Brignoli et al. 1997). Some research indicated that capillary forces only play a minor role to the water weakening effect and that alternative mechanisms should be considered(Risnes and Flaageng 1999).

Among others, possible physico-chemical mechanisms discussed are stress corrosion (Hadizadeh and Law 1991), adsorption of water on the chalk surface and the effect of water activity when changing the ion concentration of the pore fluid (Risnes, Haghighi et al. 2003, Risnes, Madland et al. 2005).

Pure chemical effects had not been focused on to the same extent. In light of discovering that physical effects and physico-chemical effects only had a smaller impact on the water weakening phenomenon, chemical mechanisms received more attention.

Substitutions of ions have been discussed as a possible explanation to the water weakening when injecting brines to the chalk (Korsnes, Madland et al. 2006,

Korsnes 2007, Madland, Hiorth et al. 2011, Øvstebø 2011). The stability of chalk is affected by the chalk mineralogy and especially the presence of calcium, magnesium and sulfate ions when injecting a fluid not in equilibrium with the chalk material. Production of calcium and loss of magnesium ions are observed through chemical effluent analysis. (Korsnes, Madland et al. 2006, Korsnes, Strand et al. 2008) proposed that ion substitution between Ca^{2+} and Mg^{2+} take place at intergranual contacts in the presence of SO_4^{2-} and that an increased temperature favors the process. But substitution of Mg^{2+} could not explain the results from research on Kansas chalk exposed to magnesium-free seawater where still enhanced weakening was observed (Madland, Midtgarden et al. 2008, Zangiabadi, Korsnes et al. 2009). Based on calculations of adsorption sites, Madland, Zangiabadi et al. (2009) also concluded that substitution mechanism could not explain the high production of calcium and retention of magnesium alone. Dissolution of some minerals and precipitation of other were discussed as a more pronounced affect, depending on where these processes would occur within the core (See chapter 2.4 for relevant chemical reactions).

Results from mechanical testing and analytical calculations performed by (Megawati, Hiorth et al. 2013) demonstrated how sulfate affects the mechanical stability of chalk by a negative surface charge that arises from adsorption of sulfate from the pore water.

2.3. CO_2 as a Tertiary Recovery Method

Chalk from the Cretaceous of the North Sea has high oil and gas capacity because of high porosity (35-45%) and low permeability (0,5-3 mD) (Risnes, Madland et al. 2005, Madland, Finsnes et al. 2006). But the chalk is also relative difficult to produce oil from. After primary production, i.e. the production of pressurized fluids, water injection as an improved oil recovery method is commonly used to maintain the reservoir pressure and to improve the macroscopic sweep efficiency in carbonate reservoirs (Madland 2005). Sea water flooding has resulted in economical viable oil recoveries. But there are still significant amounts of residual oil left, existing as bypassed zones or as capillary trapped residual oil. Injection of CO_2 into the reservoir as a tertiary recovery method to achieve enhanced oil recovery is a further option (Vuillaume, Akervoll et al. 2011).

So why is the carbon dioxide gas suitable as EOR fluid? Research upon use of CO_2 flooding has been carried out by the petroleum industry since the 1950`s and universities and governmental research centers have many projects related to it (Mungan 1984, Mungan 1991). What actually happens when CO_2 is injected into an oil reservoir is that CO_2 becomes soluble with the residual crude oil. Miscibility means that two fluids are able to mix because the interfacial tension holding the two phases apart are reduced (Norman J. Clark 1958). The mentioned process is referred to as “dynamic miscibility” (Matthews 1989). The use of CO_2 is also beneficial in terms of cost since it is less expensive than other similar miscible fluids. The reduction of capillary forces to zero enables the CO_2 to displace the oil from the pores of the rock. As a favorable consequence, the oil is pushed towards the producing well.

The residual oil will start to swell and its viscosity will be lowered, making it mobile and encountering the displacement process (Emberley, Hutcheon et al. 2005).

There are some criteria that must be fulfilled in order for CO_2 to work as an efficient EOR fluid. The pressure must be above the so-called "minimum miscibility pressure" (MMP), and also conditions like temperature and oil composition should be correct (Martin 1992). If a reservoir has undergone successful water flooding it is typically a suitable candidate also for CO_2 injection (2010).

CO_2 floods are often performed by the so called Water-Alternating-Gas model (WAG), involving alternating injection of volumes of water and volumes of gas to improve the sweep efficiency (Madland, Finsnes et al. 2006). It combines the improved macroscopic sweep of water injection with the microscopic displacement efficiency of gas (Christensen, Stenby et al. 2001).

CO_2 also has the potential of being used for enhanced oil recovery by injection combined with carbon dioxide capture and storage (CCS), which has attract great interest considering the dramatic increase of carbon dioxide concentration in the atmosphere due to a significant increase in fossil fuel consumption and CO_2 emission. The increased emission of the greenhouse gas CO_2 in particular is believed to be responsible for the rise in global temperature leading to glacial melting and rising sea level, and also the acidification of the ocean which in turn will harm the marine ecosystem. The possibility of CO_2 capture coupled with sequestration in deep geological formation has emerged in attempt to reduce those problems. The main storing options include coal beds, saline aquifers and depleted oil and gas reservoirs (Bachu 2000). The fate of the injected CO_2 and the mechanisms of how the gas is trapped in deep sedimentary basins include physical or chemical trapping processes

(Gunter, Bachu et al. 2004, Bachu 2008, Benson and Cole 2008, Gaus, Audigane et al. 2008). Physical trapping are static trapping in structural or stratigraphic traps were supercritical CO_2 are trapped as a buoyant immiscible fluid phase or residual-gas trapping in small pores where the supercritical CO_2 is not mobile any more. Chemical trapping represent dissolved CO_2 in the liquid phase of oil or brines, known as dissolution trapping. If the dissolved CO_2 is incorporated into minerals through precipitation processes, the chemical process is termed mineral trapping.

Oil and gas reservoirs have the ability to retained hydro carbons for millions of years because of the geologic seals they possess, and are therefore good candidates for CO_2 storage (Gozalpour, Ren et al. 2005). Besides the confinement, geological media for CCS also have suitable capacity and injectivity to accept the large volumes of CO_2 (Bachu 2008).

There are two ongoing CO_2 storage projects on the Norwegian sector, both in sandstone formations. CO_2 from the Sleipner field has been stored in the Utsira formation since October 1996 (Arts, Eiken et al. 2004), and CO_2 from the Snøhvit field in the Barents Sea are stored in the Tubåen formation (2008). The storage sites are being carefully monitored, and there have not been any unexpected movement of the reservoir observed or indication of leakage. But there have been registered a pressure buildup in parts of the Tubåen formation as a result of the injected CO_2. Although storage in the mentioned sandstone formation has so far been successful, studies from the more comprehensive CO_2 storage project, the In Salah project, in Algeria have reported geomechanical changes (Rutqvist, Vasco et al. 2010). Identifying other possible formations on the Norwegian continental shelf that are suitable for long term storage of CO_2 is in progress (2011). Careful and explicit research should be performed upon carbonate rock formations in order to evaluate

whether this particular type of formation is suitable as long-term storage site. The Weyburn oil field is a mature carbonate reservoir in Canada. CO_2 injection for EOR was initiated in 2000, and it has been studied and monitored to evaluate the possibility for permanent CO_2 storage (Verdon, Kendall et al. 2013). Emberley, Hutcheon et al. (2005) indicated that the injected CO_2 lowers the pH which probably causes dissolution of carbonate minerals (calcite and dolomite) in the reservoir. However, they also mention that *"there is some evidence to support the potential that fluids in the reservoir also are reacting with the trace amounts of silicate minerals. If correct, the silica minerals may be capable of buffering pH and causing thereby the precipitation of injected CO_2 as calcite over longer time periods, probably of the order of thousands of years."*

Even though compaction is one of the driving mechanisms in extracting oil from the pore space, engineers today are well aware of the detrimental effects of uncontrolled reservoir compaction. Loss in pore volume may reduce the permeability of the reservoir, buckling of pipes may lead to loss of equipment and reservoir compaction may induce additional sea bed subsidence. Therefore, many questions regarding the impact on reservoir integrity must be addressed in order to predict the long term effects of CO_2 sequestration. How the porosity and permeability of the rock will evolve, if the injection of carbon dioxide will result in even stronger deformation and if this in turn will influence cap rock and fault seal integrity are all current questions (Liteanu and Spiers 2009).

2.4. The Chemistry of CO_2 and Sea Water in Relation to Chalk Material

CO_2 is not only miscible with crude oil, but also with formation water in the reservoir and with injected sea water. When gaseous CO_2 comes into contact with sea water or formation water it will dissolve into the brine, forming carbonic acid and subsequently bicarbonate in the reservoir. The sour conditions that arise will increase the calcite solubility as solubility of carbonates is strongly pH dependent:

$$CO_{2\,(g)} \leftrightarrow CO_{2\,(aq)} \qquad \text{(Eq. 2-1)}$$

$$CO_{2\,(aq)} + H_2O_{\,(l)} \leftrightarrow [H_2CO3_{\,(aq)}] \leftrightarrow HCO3^-_{(aq)} + H^+_{\,(aq)} \qquad \text{(Eq. 2-2)}$$

$$CaCO3_{(s)} + H_2O_{\,(l)} \leftrightarrow Ca^{2+}_{\,(aq)} + HCO_3^-{}_{\,(aq)} + OH^-_{\,(aq)} \qquad \text{(Eq. 2-3)}$$

The following overall chemical reaction can be used to describe the interactions when CO_2 is injected into a carbonate aquifer:

$$CaCO3_{\,(s)} + CO_{2\,(aq)} + H_2O_{\,(l)} \leftrightarrow Ca^{2+}_{\,(aq)} + 2HCO_3^-{}_{\,(aq)} \qquad \text{(Eq. 2-4)}$$

Since the solubility of gaseous CO_2 in water is govern by the partial pressure, temperature and brine composition, high levels of P_{CO2} will drive (Eq. 2-1) to the right according to Le Chateliers´s principle. Consequently, the pH decreases and the concentration of dissolved calcium and bicarbonate ions in the pore water increase. An increase in temperature and ionic strength will have the opposite effect, leading to lower solubility of gaseous CO_2 in the water, thus smaller amount of calcite dissolution.

Dissolved bicarbonate ions can further react with cat ions present in sea water like Mg^{2+} and Ca^{2+} to form other stable carbonates:

$$Ca^{2+}_{(aq)} + HCO_3^-{}_{(aq)} \leftrightarrow CaCO_{3\,(s)} + H^+_{(aq)} \quad \text{(Eq. 2-5)}$$

$$Mg^{2+}_{(aq)} + HCO_3^-{}_{(aq)} \leftrightarrow MgCO_{3\,(s)} + H^+_{(aq)} \quad \text{(Eq. 2-6)}$$

The increased amount of calcium ions from the dissolution of chalk can react with sulfate ions in the sea water and precipitate $CaSO_{4\,(s)}$:

$$Ca^{2+}_{(aq)} + SO_4^{2-}{}_{(aq)} \leftrightarrow CaSO_{4\,(s)} \quad \text{(Eq. 2-7)}$$

If calcium ions or carbonate ions are removed chemically by reacting with other ions present, the equilibrium of the solution will be altered. Again, this can be explained by Le Chateliers´s principle: If the concentration of an ion decreases, the position of the equilibrium will move in the direction that increases the concentration of the ion again. In this case, promote even more dissolution of chalk. We can say that the water-weakening effect becomes even stronger, which has an impact on the mechanical strength of the rock. Investigation of how dissolved CO_2 alters the integrity of the reservoir rock is therefore significant knowledge when considering production strategies and potential carbon storage sites (CSS) of chalk reservoirs.

Various experimental researches have been conducted to investigate how CO_2 will influence the behavior of chalk (Madland, Finsnes et al. 2006, Kaufmann and Dreybrodt 2007, Le Guen, Renard et al. 2007, Korsnes, Madland et al. 2008, Liteanu and Spiers 2009, Alam 2011, Grgic 2011, Kvinge 2012, Ahmed 2013, Liteanu, Spiers et al. 2013).

While the study performed by Liteanu, Spiers et al. (2013) showed no significant short-term effects on wet chalk from injection of supercritical CO_2, experimental results from Madland, Finsnes et al. (2006) and Korsnes, Madland et al. (2008)comparing strain rates of stressed chalk cores flooded with and without CO_2 enriched brines at ambient temperature indicated weakening effects. The strain rates

reported from Korsnes, Madland et al. (2008) show that the strain rates had increased with a factor between 1.5 and 3.3 when CO_2 was present in the brines. These results are higher by an average factor of 1.6 than what is reported by Madland, Finsnes et al. (2006). Even though the two studies are comparable based on chalk type, temperature, creep stress and fluid composition, Madland, Finsnes et al. (2006) performed the experiments without backpressure. The partial pressure of CO_2 is reduced gradually as carbonated water is flooded through the core, resulting in lower solubility of CO_2 and lower dissolution of chalk. Thus, lower strain rates than with backpressure.

Le Guen, Renard et al. (2007) reported that fluids with a high partial pressure of CO_2 induced accelerating creep effect in limestone. They explained it by the acidification of the injected fluid which increases the calcite dissolution and reaction kinetics.

2.5. Carbonate Rock; Chalk

Important sedimentary rocks when considering reservoir rocks are the carbonated ones. A survey from 2013 performed by Schlumberger estimated that that more than 60 % of the world's oil reserves and 40 % of the world's gas reserves are held in carbonate reservoirs (2013). Carbonate rocks can be subdivided into groups based on their crystal system. Chalk belongs to the group limestone and has maintained its biogenic origin. It is a white and porous fine-grained material with a soft matrix that mainly consists of the mineral calcite (Roehl and Choquette 1985). The chalk is made of whole and fragmentary parts of calcite skeletons produced by planktonic algae. The skeleton consists of calcite platelets and tablets of the average size 1μm arranged in rings called coccolith rings with a diameter of 3-15 μm (Røgen and Fabricius 2002).

The relatively open structure of the chalk and the coccolith rings can be observed in the scanning electron microscope (SEM) picture of Kansas outcrop chalk presented in Figure 2-1.

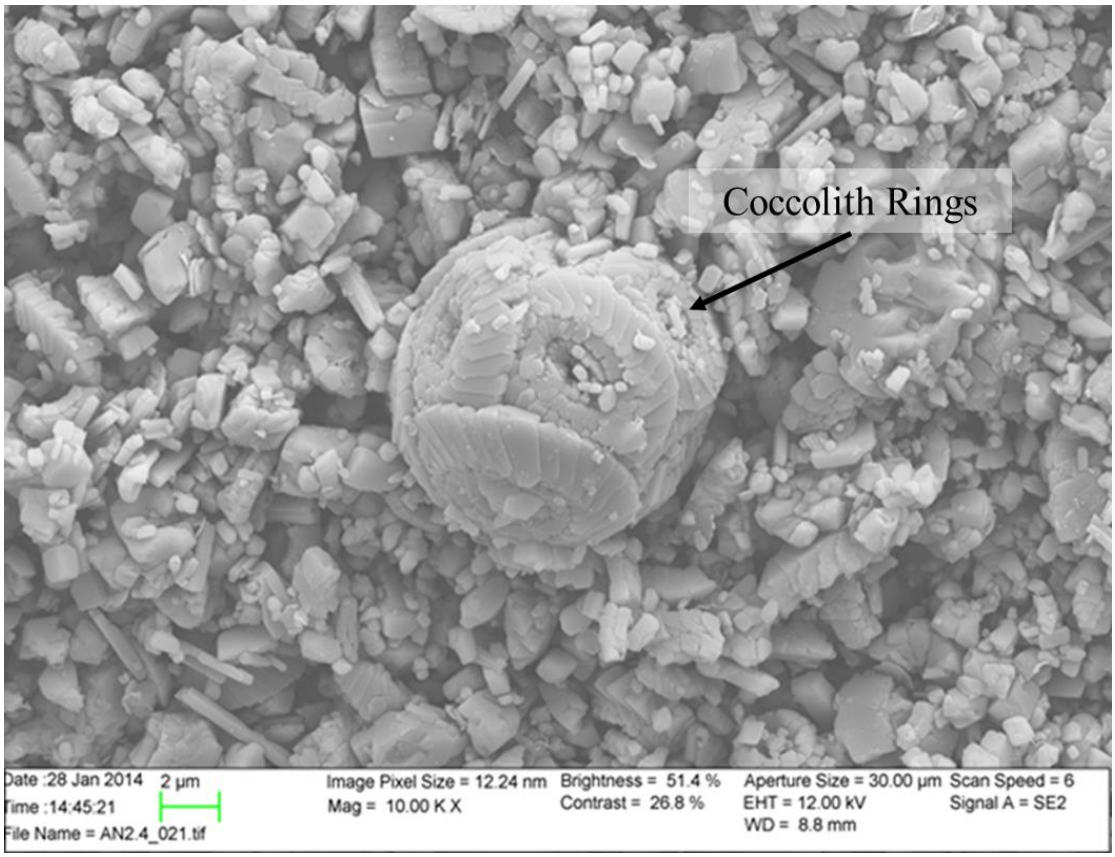

Figure 2-1: SEM image of Kansas chalk.

2.6. Mechanical Properties of Chalk

2.6.1. STRESS

Stress is generally defined as force per unit area:

$$\sigma = \frac{F}{A} \qquad \text{(Eq. 2-8)}$$

Where σ is the stress, F is the force [N] and A is the cross-section [m^2]. Stress is measured in Pascal [Pa] in the SI-system, which is equivalent to [Nm^2], but can also be presented in units like psi, bars, atmosphere, dynes/cm^2.

2.6.1.1. Axial Stress

Forces can be exerted in axial or radial direction on a cylinder, Figure 2-2.

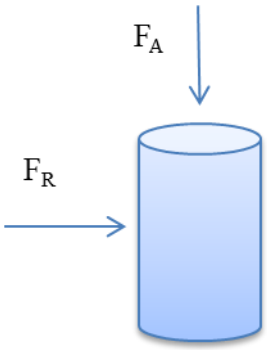

Figure 2-2: Axial and radial forces exerted on the surface of a cylinder.

Axial stress is generally defined as:

$$\sigma_A = \frac{F_A}{\pi r^2} \qquad \text{(Eq. 2-9)}$$

Where σ_A is the axial stress and F_A is the axial forces exerted on the cylinder with a radius r. Axial stress is calculated from the radial stress (σ_R), piston pressure (p_{Piston}),

frictional pressure ($p_{Friction}$) and conversion factor (f_{Area}). This stress is also termed overburden stress (σ_{OB}) and can be calculated from the following equation:

$$\sigma_A = \sigma_R + f_{Area}(P_{Piston} - P_{Friction}) = \sigma_{OB} \quad \text{(Eq. 2-10)}$$

2.6.1.2. Differential Axial Stress

Differential stress (σ_D) in axial direction is defined as the axial stress (σ_A) exerted to the grains minus the fluid pressure inside the pores of the material, called pore pressure (P_P):

$$\sigma_D = \sigma_A - P_P \quad \text{(Eq. 2-11)}$$

2.6.1.3. Effective Stress Relation

The effective stress (σ_E) is given by the overburden stress (P_{OB}) minus a fraction $\boldsymbol{\alpha}$ of the pore pressure (P_p):

$$\sigma_E = P_{OB} - \alpha P_p \quad \text{(Eq. 2-12)}$$

2.6.2. STRAIN

Mechanical strain is the deformation of a material caused by stress. Strain is dimensionless and can be elastic or plastic. Elastic strain refers to strain where the material can return to its original state when the applied stress is removed. The material has the ability to recover. Plastic strain is irreversible, meaning that the exerted forces are greater than the internal stress of the material.

2.6.2.1. Axial Strain

Figure 2-3 illustrates the length (L) of the cylinder at original state and the length (L') of the deformed cylinder as a result of applied stress in axial direction.

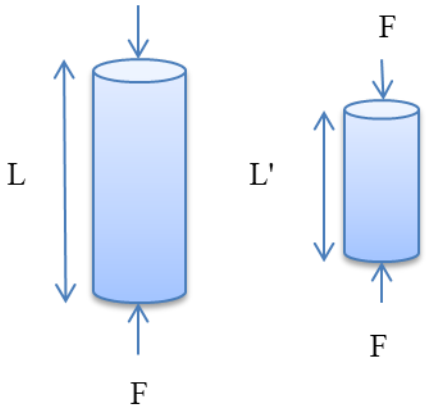

Figure 2-3: Axial stress deformation due to axial force, F

Axial strain at time *(t)* can be defined as:

$$\varepsilon_A(t) = \frac{\Delta L}{L_0} = \frac{L(t)-L_0}{L_0} \qquad \text{(Eq. 2-13)}$$

Where L_0 is the initial length of the material, $L(t)$ is length of the material at time *(t)* and ΔL is the difference between $L(t)$ and L_0. (Eq. 2-13 can be written as:

$$L(t) = L_0(\varepsilon_A(t) + 1) \qquad \text{(Eq. 2-14)}$$

2.6.2.2. Radial Strain

Radial strain at time (t) can be defined as:

$$\varepsilon_R(t) = \frac{\Delta R}{R_0} = \frac{R(t)-R_0}{R_0} \quad \text{(Eq. 2-15)}$$

Where R_0 is the radius of the material at the initial time, $R(t)$ is the radius of the material at time (t) and ΔR is the difference between $R(t)$ and R_0. (Eq. 2-15 can be written as:

$$R(t) = R_0(\varepsilon_R(t) + 1) \quad \text{(Eq. 2-16)}$$

2.6.2.3. Volumetric Strain

Volumetric strain at time (t) can be defined as:

$$\varepsilon_V(t) = \frac{\Delta V}{V_0} = \frac{V(t)-V_0}{V_0} \quad \text{(Eq. 2-17)}$$

Where V_0 is the volume of the material before testing, $V(t)$ is the volume of the material at time (t) and ΔV is the difference between $V(t)$ and V_0. The volume V of a cylinder is defined by:

$$V = \pi R^2 L \quad \text{(Eq. 2-18)}$$

Where R is the radius of the cylinder and L is the length.

Inserting Eq. 2-14, Eq. 2-16 and Eq. 2-18 give into Eq. 2-17 give:

$$\varepsilon_V(t) = (\varepsilon_R(t) + 1)^2(\varepsilon_A(t) + 1) - 1 \quad \text{(Eq. 2-19)}$$

Under uniaxial condition, ε_R(t) is zero. Thus, we can wright:

$$\varepsilon_V(t) = \varepsilon_A(t) \qquad \text{(Eq. 2-20)}$$

2.6.3. STRESS-STRAIN RELATIONSHIP

At low stresses there is a linear relationship between the applied stress and observed strain. The onset of yield is determined from the point where the stress-strain curve starts to deviate from the linear trend, illustrated in Figure 2-4. The area before onset of yield is the elastic area where the deformation is reversible, although permanent deformation may also be observed at low stresses. E-modulus is a measurement of the stiffness of the material. Within the elastic area, E-modulus is given directly from the slope of the curve.

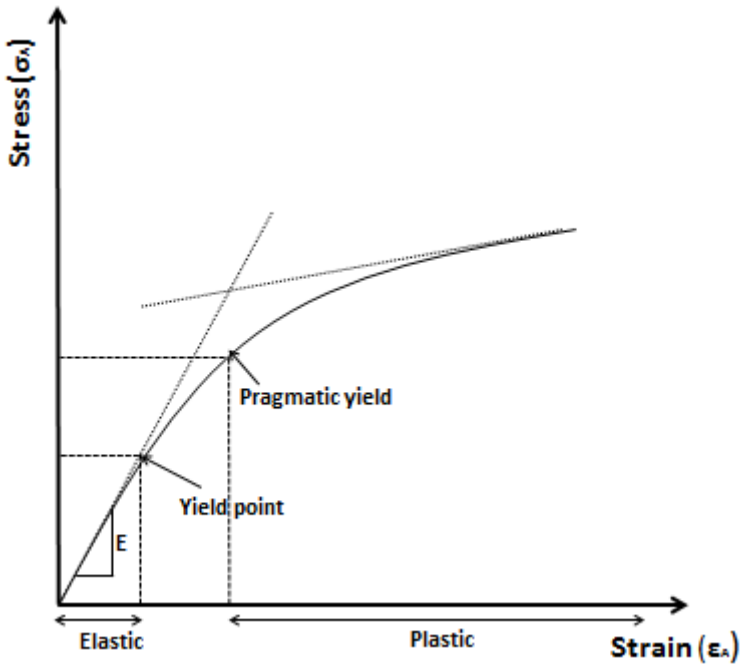

Figure 2-4: Axial stress plotted as a function of axial strain for a test under uniaxial strain conditions

As the plug continues to deform it reaches the pragmatic yield. The area from onset of yield to pragmatic yield is termed the transitional area. The elastic axial stress (σ_A^{el}) equals the plastic elastic stress (σ_A^{pl}) at pragmatic yield:

$$\sigma_A^{el} = \sigma_A^{pl} \quad \text{(Eq. 2-21)}$$

σ_A^{el} and σ_A^{pl} is defined by:

$$\sigma_A^{el} = K_A^{el}\varepsilon_A + \sigma_{A,0}^{el} \quad \text{(Eq. 2-22)}$$

$$\sigma_A^{pl} = K_A^{pl}\varepsilon_A + \sigma_{A,0}^{pl} \quad \text{(Eq. 2-23)}$$

Where K_A^{el} and K_A^{pl} are the slope of the elastic and plastic strain curve, respectively.

Inserting (Eq. 2-22 and (Eq. 2-23 into (Eq. 2-21 and rearranging the equation, the axial strain at pragmatic yield is given by:

$$\varepsilon_A = \left(\frac{\sigma_{A,0}^{pl} - \sigma_{A,0}^{el}}{(K_A^{el} - K_A^{pl}}\right) \quad \text{(Eq. 2-24)}$$

2.6.4. CREEP

Creep is defined as time dependent deformation that occurs under constant stress and temperature conditions. Creep can be divided into three stages as shown in Figure 2-5. The first phase is the transient creep (primary creep) where deformation decreases with time. The second period is the steady state creep (secondary creep) where the deformation of material is constant and permanent. There may also be a third phase called accelerating creep if the deformation rate increases with time (Fjær et al. 2008).

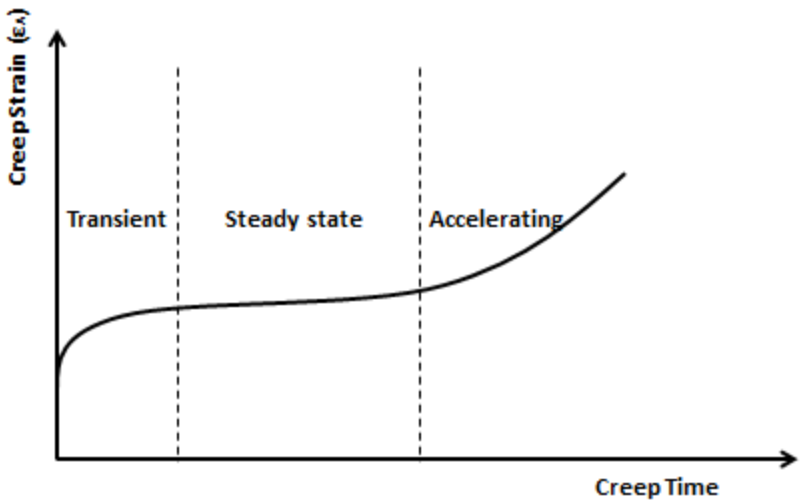

Figure 2-5: Material under creep conditions. Axial creep strain is plotted as a function of creep time.

Evaluation of how the material responds to changes in pore fluid composition through time and how this alters the creep curve is fitted using a statistical parameterization. Our experiments comprise different stages that give us thousands of measurements of the strain through time. Fitting the experimental results into a statistical parameterization enables us to condense the thousands of measurements to two model

parameters. We found that the Power law model fitted our results to a satisfying degree, although several other models may also be relevant. The Power law can be expressed by the following equation:

$$\varepsilon_A(t) = At^B \quad \text{(Eq. 2-25)}$$

Where $\varepsilon_A(t)$ is the strain at time (t), t is the time and A and B are fitting parameters. A and B are altered according to the different brine compositions the core is flooded with in order to adapt the power law model to the observed strain curve.

The power law parameterization is not a good fit for accelerating creep areas. The square time dependency fitted our results to a better degree:

$$\varepsilon_A(t) = At^2 \quad \text{(Eq. 2-26)}$$

2.6.5. PERMEABILITY

Permeability describes the ability of a fluid to flow through a permeable material. The SI unit for permeability is square meter (m^2), but the units Darcy (D) or millidarcy (mD) is common used. Permeability is governed by Darcy's Law:

$$K = \frac{qL\mu}{A\Delta P} \quad \text{(Eq. 2-27)}$$

Where q is the flow rate of the fluid (cm^3/s), L is the length of the core (cm), μ is the fluid dynamic viscosity (cP), A is the cross section area of the core (cm^2) and ΔP is differential pressure (atm). Thus, the unit of the permeability K is given in Darcy (D).

2.6.6. POROSITY

Porosity is a measure of the void space in the rock. Chalk is a porous material, consisting of solid material and void space based on the arrangement of the solid grains. The bulk volume V_B is the sum of the solid volume V_S of the material and the pore volume V_P:

$$V_B = V_S + V_P \quad \text{(Eq. 2-28)}$$

Porosity ϕ can be defined as:

$$\Phi = \frac{V_P}{V_B} \quad \text{(Eq. 2-29)}$$

From (Eq. 2-29 porosity can be calculated in different ways.

1. The pore volume or void volume V_P can be defined as:

$$V_P = \frac{W_W - W_D}{\rho_{dw}} \quad \text{(Eq. 2-30)}$$

Where the density of distilled water ρ_{dw} is $1^{g}/_{ml}$, W_W is the weight of the core when saturated with distilled water and W_D is the dry weight of the core. The bulk volume V_B can be calculated from the following equation by measuring the diameter D and length L:

$$V_B = L\pi\left(\frac{D}{2}\right)^2 \quad \text{(Eq. 2-31)}$$

Inserting (Eq. 2-30 and (Eq. 2-31 into (Eq. 2-29 give:

$$\Phi = \frac{W_W - W_D}{L\pi\left(\frac{D}{2}\right)^2} \quad \text{(Eq. 2-32)}$$

2. Measuring the density ρ_s of the solid material in the pycnometer enable us to calculate the solid volume V_s from the following equation:

$$V_S = \frac{W_D}{\rho_S} \qquad \text{(Eq. 2-33)}$$

Inserting (Eq. 2-28 and (Eq. 2-33 into the porosity definition in (Eq. 2-29, we find that:

$$\phi = \frac{V_P}{V_B} = \frac{V_B - V_S}{V_B} = 1 - \frac{\left(\frac{W_D}{\rho_S}\right)}{V_B} \qquad \text{(Eq. 2-34)}$$

3. Porosity in our experiments changes over time. Porosity at time (t) is defined as:

$$\phi(t) = \frac{V_P(t)}{V_B(t)} \qquad \text{(Eq. 2-35)}$$

Considering porosity evolution over time, the definition of porosity at time (t) can be defined as:

$$\phi(t) = \frac{V_{P0} + \Delta V_P(t)}{V_{B0} + \Delta V_B(t)} \qquad \text{(Eq. 2-36)}$$

Writing (Eq. 2-28 also in respect of change over time (t):

$$\Delta V_P(t) = \Delta V_B(t) - \Delta V_S(t) \qquad \text{(Eq. 2-37)}$$

Inserting (Eq. 2-37 into (Eq. 2-36, gives:

$$\phi(t) = \frac{V_{P0} + (\Delta V_B(t) - \Delta V_S(t))}{V_{B0} + \Delta V_B(t)} \qquad \text{(Eq. 2-38)}$$

From the definition of volumetric strain in (Eq. 2-17 and the definition of porosity in (Eq. 2-29 we find that:

$$\phi(t) = \frac{\phi_0 + \varepsilon_V(t) - \left(\frac{\Delta V_S(t)}{V_{B0}}\right)}{1 + \varepsilon_V(t)} \qquad \text{(Eq. 2-39)}$$

Under the assumption that all strain is volumetric strain by pore collapse due to reorganization of the grains when flooding with fluids that will not affect the chemical equilibrium of the chalk, $\Delta V_S(t)$ is zero and porosity is expressed by:

$$\phi(t) = \frac{\phi_0 + \varepsilon_V(t)}{1 + \varepsilon_V(t)} \qquad \text{(Eq. 2-40)}$$

When flooding with non-equilibrium fluids, chemical fluid-rock interactions should also be considered. The precipitation/dissolution processes that we keep track of through effluent sampling will affect the solid volume change over time *ΔVs(t)*:

$$\Delta V_S(t) = \frac{M_S(t)}{\rho_S(t)} - \frac{M_{S0}}{\rho_{S0}} \qquad \text{(Eq. 2-41)}$$

Inserting (Eq. 2-41 into (Eq. 2-39 gives:

$$\phi(t) = \frac{\phi_0 + \varepsilon_V(t) - \frac{1}{V_{B0}}\left(\frac{\Delta M_S(t)}{\Delta \rho_S(t)} - \frac{M_{S0}}{\rho_{S0}}\right)}{1 - \varepsilon_V(t)} \qquad \text{(Eq. 2-42)}$$

2.6.7. STRAIN PARTITIONING

When the core is flooded with a non-equilibrium fluid the observed strain is a function of not only pore collapse, but also chemical rock-fluid interactions. By the term *strain partitioning* we mean how much of the observed strain that can be explained by mechanical strain versus chemical strain, where mechanical strain is referred to as pore collapse *(ε_P)* and chemical strain is dissolution/precipitation processes *(ε_S)*. In the simplest form the relationship between the observed total strain, mechanical strain and chemical strain can be expressed by:

$$\varepsilon_{Total} = \varepsilon_P + \varepsilon_S \qquad \text{(Eq. 2-43)}$$

How the total volume consists of both solid volume and pore volume is illustrated in Figure 2-6. Through deformation, these volumes changes with time.

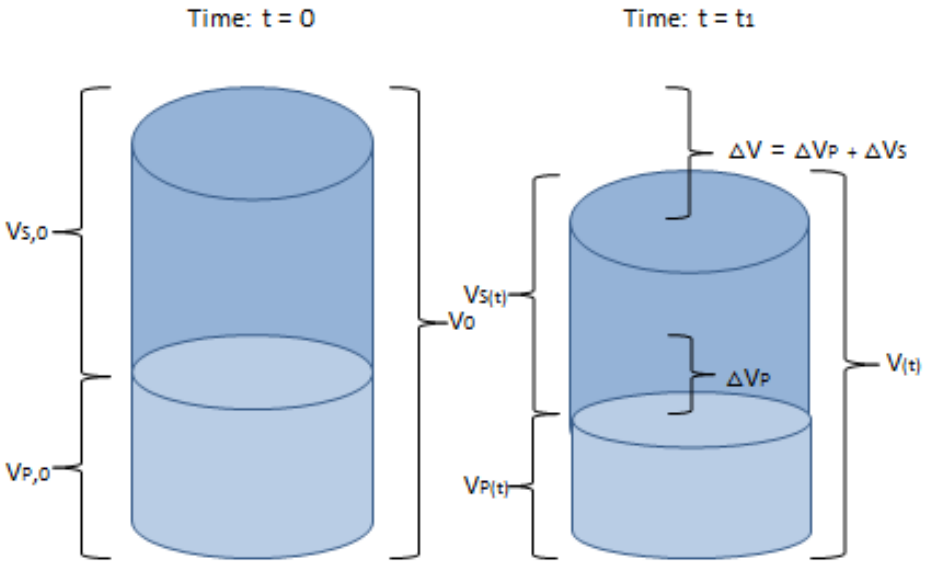

Figure 2-6: The relationship between pore volume changes and solid volume changes over time through strain partitioning.

The total volume consists of solids and pores as illustrated in Figure 2-6. Through deformation, these volumes changes with time such that the total volumetric deformation is the sum of the pore volume change plus the solid volume change,

The change in solid volume ΔV_s at a given time (t) can be calculated from the definition of volumetric strain in (Eq. 2-17 and (Eq. 2-41:

$$\varepsilon_S = \frac{\Delta V_P}{V_{B0}} + \frac{\Delta V_S}{V_{B0}} \qquad \text{(Eq. 2-44)}$$

As stated above, we assume that the mechanical strain is associated with the pore volume development ($\varepsilon_{mech} = \varepsilon_p$) and the chemical strain to solid volume change ($\varepsilon_{chem} = \varepsilon_S$). This does not necessary mean that the causal origin of the pore volume change has a pure mechanical origin, and vice versa, that the causal origin in the solid volume change has a pure chemical origin. It has been observed that a rapid reduction in porosity (i.e. pore space reduction) may be induced by the chemistry of the pore fluid, and vice versa the rate of dissolution/precipitation can be controlled by the induced mechanical stresses. As such, more complicated strain partitioning may be developed in the future. Here we employ the simplest form of strain partitioning. The change in solid volume ΔV_s at a given time (t) can be calculated from the mass and the density at any given time:

$$\varepsilon_S = \frac{\Delta V_S}{V_{t,0}} = \frac{\left(\frac{M_S(t)}{\rho_S(t)}\right) - \left(\frac{M_{S0}}{\rho_{S0}}\right)}{\left(\frac{M_{S0}}{\rho_{S0}}\right)} \qquad \text{(Eq. 2-45)}$$

The initial solid mass M_{S0} of the plug is measured on a scale, while the solid mass at time (t) is calculated based on the ion concentrations from the ionic

chromatography test results. Densities before and after test are estimated with a pycnometer (*Micromeritics Gas Pycnometer model AccuPyc II 1340*).

Knowing the total observed strain and from calculating the chemical strain, we can also estimate the mechanical strain from (Eq. 2-43, to evaluate how much of the observed total strain that is chemical or mechanical contribution.

2.6.8. Q-P DIAGRAMS

A q-p' diagram as shown in Figure 2-7 is one way of presenting yield and failure data, by showing the failure envelop and making it easier to trace the stress path of the experiment. The generalized shear stress in a cylindrical sample is expressed as follows:

$$q = \sqrt{(\sigma_{A-}\sigma_R)^2} \qquad \text{(Eq. 2-46)}$$

Where σ_A is the applied stress in radial direction and σ_R is the applied stress in axial direction. The stress in axial direction used in the calculations is the axial differential stress and the confining pressure represents the applied stress in radial direction. The average effective stress p' is defined by:

$$p' = \frac{\sigma_{A+2\sigma_R}}{3} - p_P \qquad \text{(Eq. 2-47)}$$

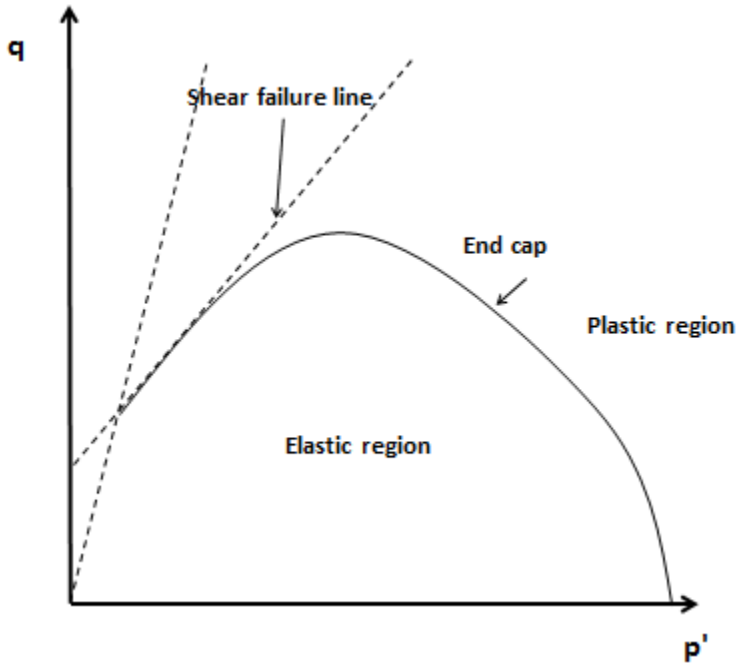

Figure 2-7: Example of how a typical Q-P plot looks like.

3. MATERIAL AND METHODES

3.1. Test Material

High porosity outcrop chalk from the quarry of Kansas in Niobrara, US, has been used as test material in all three experiments. The three cores are named KA9-L, KA24-L and KA28-U. Each core drilled from the chalk block is cut into to two smaller cores to fit the triaxial cell. The L and U stand for Lower and Upper to indicate if it is the lower or upper part of the drilled core bit. Number 9, 24 and 28 is the number of cores drilled out from the chalk block.

3.2. Test Equipment

An oversized core was first drilled out from a block of Kansas outcrop chalk by a drilling machine (Figure 3-1). A lathe machine (Figure 3-2) was used for polishing and shaping the core into the desirable diameter of approximately 37 and 38 mm. The next step was to cut the oversized core into two shorter cores with the appropriate length of approximately 70mm (Figure 3-3). End pieces after cutting were saved for comparison with the flooded core after test.

Figure 3-1: The drilling machine used for drilling the cores out from the Kansas chalk block.

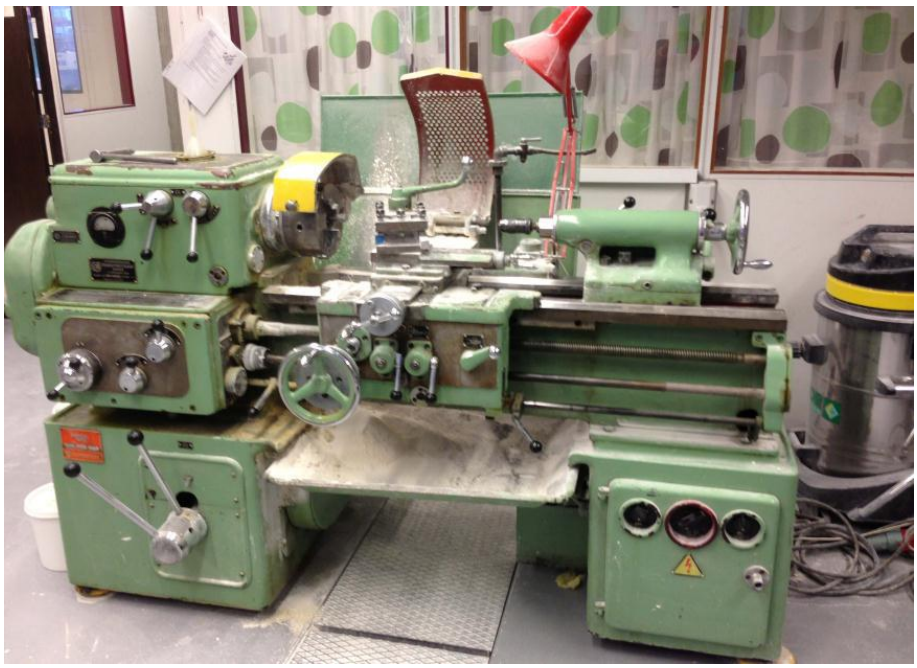

Figure 3-2: The turning lathe machine

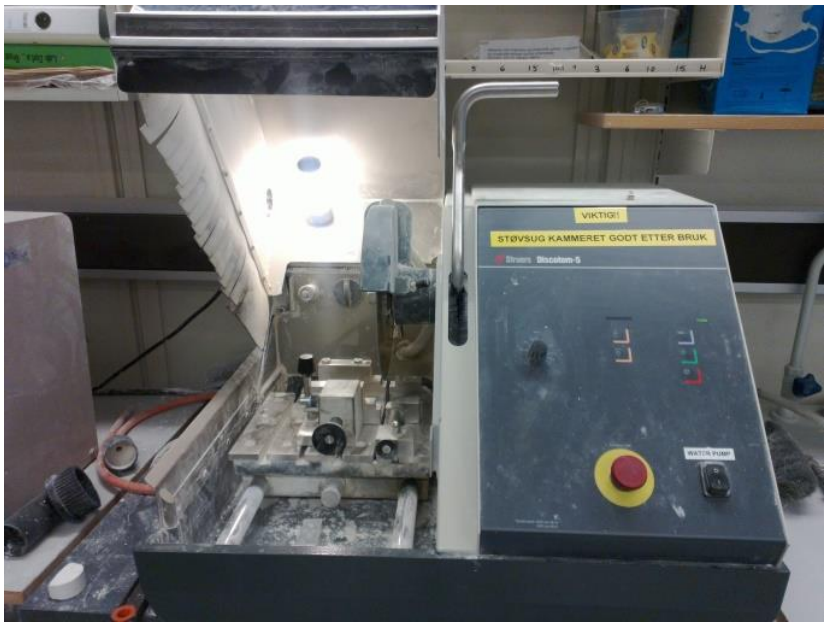

Figure 3-3: The cutting machine

The core was dried in a heating chamber to evaporate all water. The dry weight was measured on a scale while the length and diameter was measured by a sliding caliper. The core was saturated with distilled water in a vacuum chamber in order to estimate the porosity (Figure 3-4). Then the wet weight of the core was then measured on a scale. All equations involved in estimating the porosity are given in chapter 2.6.6.

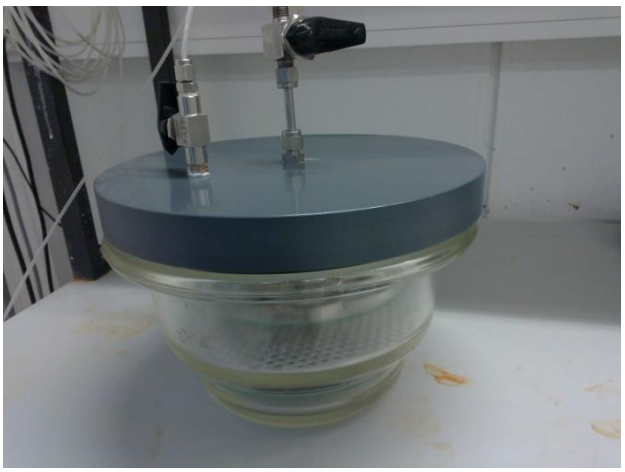

Figure 3-4: Vacuum chamber.

3.3. Experimental Preparation

The tests are performed in a high pressure, high temperature (HPHT) triaxial cell. A schematic figure is illustrated in Figure 3-5 and a picture of the traxial cell during testing is shown in Figure 3-6.

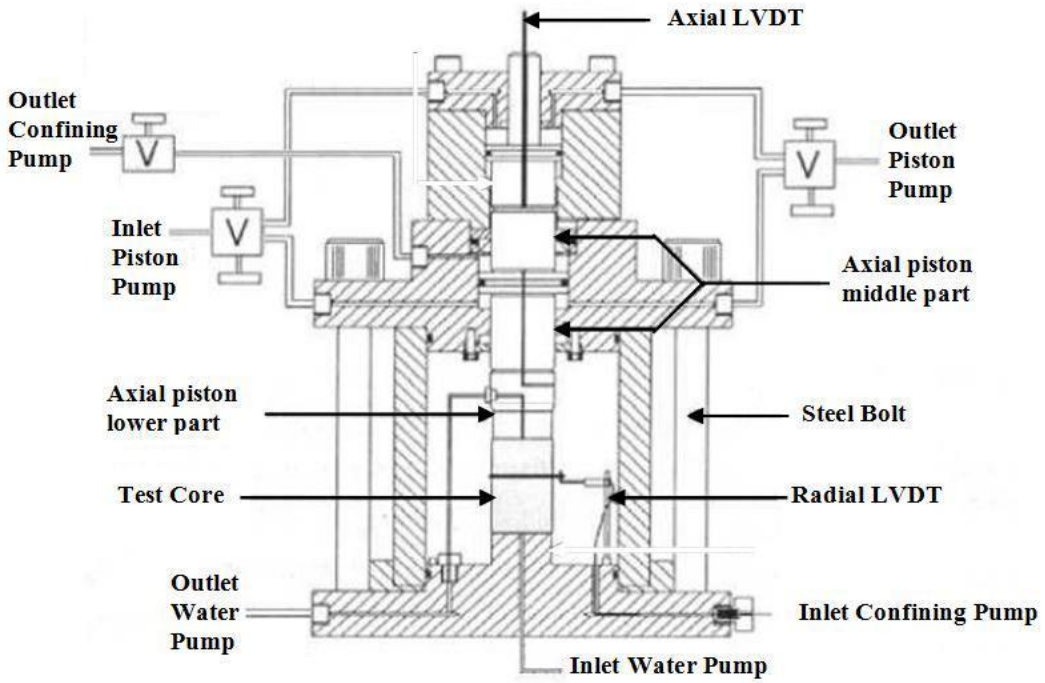

Figure 3-5: HPHT triaxial cell

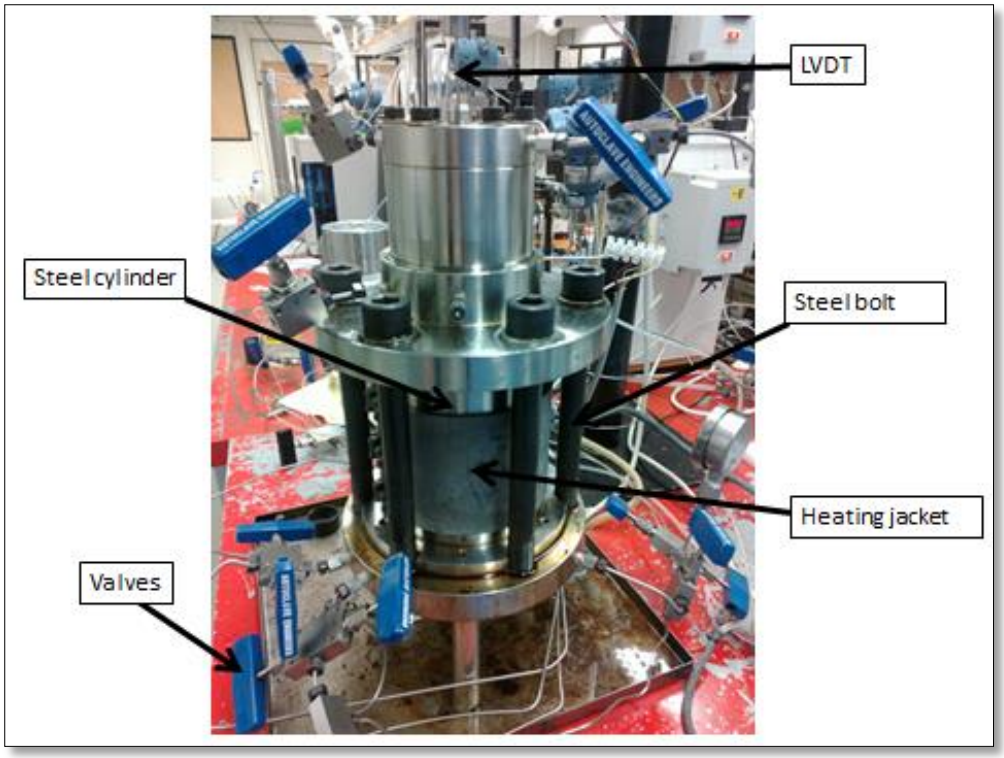

Figure 3-6: Triaxial cell setup

The triaxial cell is equipped with several pumps. The high pressure Gilson Pump, Model 307 HPLC, (Figure 3-7) controls the flow rate of the injected fluid. Piston pressure and confining pressure are controlled by the Quizix Pumps, Model QX-20000 HC (Figure 3-8). The pore pressure is controlled by a backpressure regulator in the KA9-L and KA24-L tests. But in the KA28-U test is the pore pressure controlled by the Teledyne Isco Syringe Pump, Model 260D.

The computer software Labview enable us to log valuable information during the experiment, operate pumps, monitor the different stresses, the flooding rate, elapsed time etc.

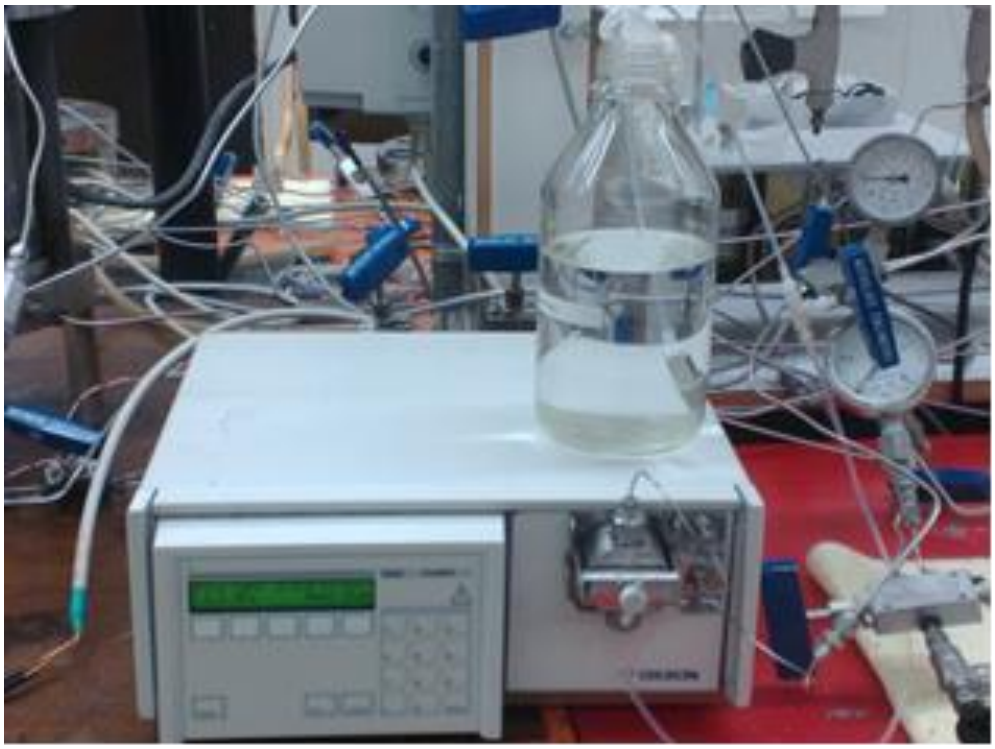

Figure 3-7: The Gilson pump, Model 307 HPLC

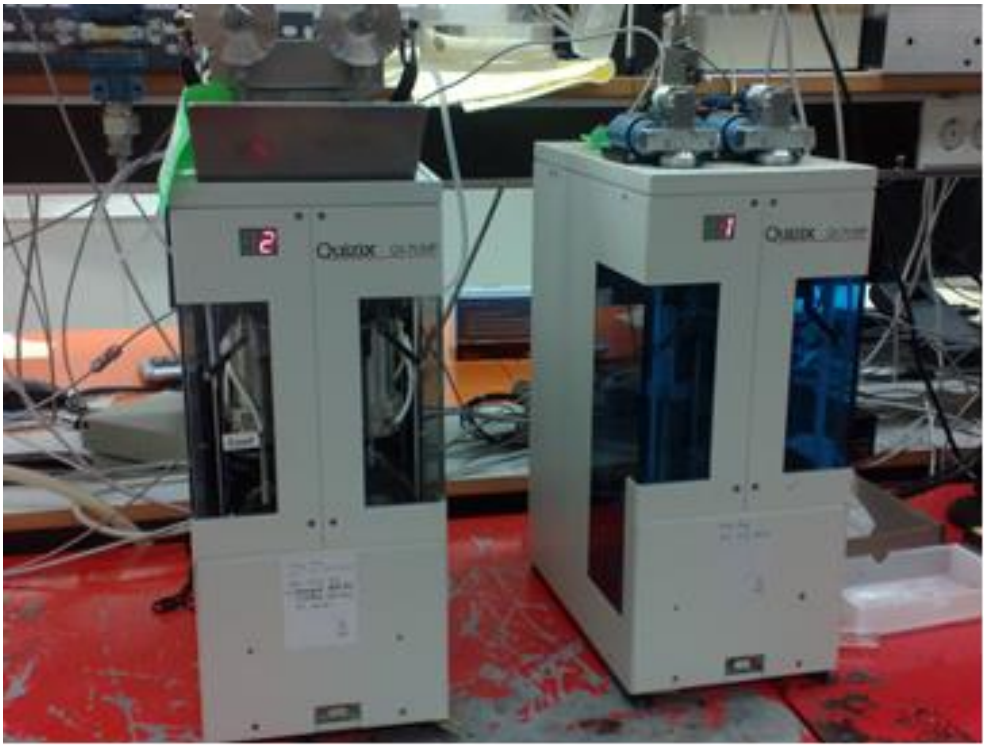

Figure 3-8: Quizix Pumps, Model QX-20000 HC

The temperature is regulated by a heating jacket surrounding the cell. The position of the piston is monitored by a Linear Voltage Displacement Transducer (LVDT) and the circumferential distance is monitored by an extensometer. We can calculate the axial deformation in Eq. 2-13 from the LVDT measurement of the length. The strain in radial direction, which should be zero under uniaxial conditions, is calculated from Eq. 2-15 and the measurements from the extensometer.

The flooding fluid are stored in a flooding cell (Figure 3-9) and circulated into the triaxial cell. There are two separate chambers inside the flooding cell with a movable piston between. The water pump is connected to the upper chamber. Distilled water is pumped into the upper chamber of a piston cell pushing the flooding fluid in the lower chamber into the triaxial cell and the chalk core.

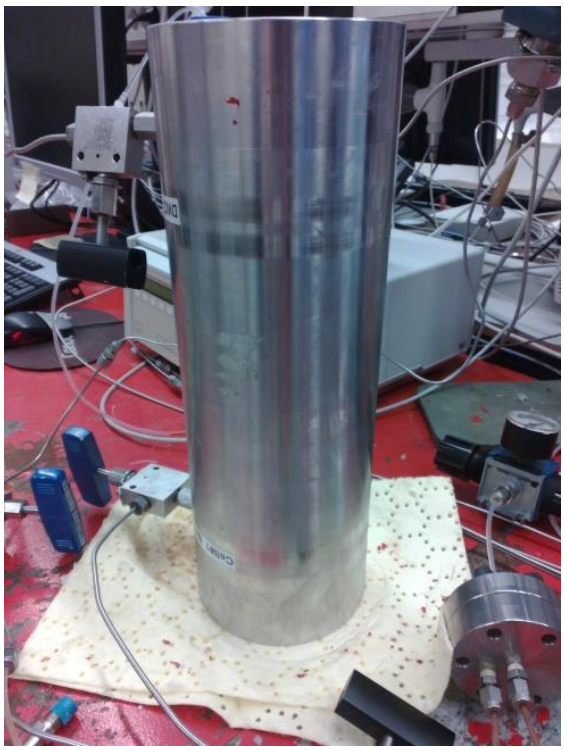

Figure 3-9: The piston cell used for flooding.

The solid volume and standard deviation are measured by an Accu Pyc II Gas Pycnometer (Figure 3-10) after cutting the core into smaller pieces. Helium gas was used during testing. The density can be calculated from the solid volume and dry weight measurements.

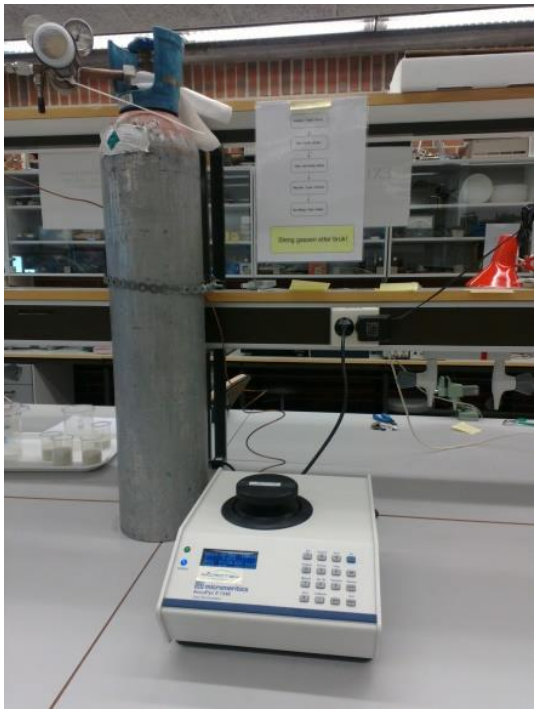

Figure 3-10: Micromeritics Gas Pycnometer model AccuPyc II 1340

The core needs to be cut into smaller pieces prior to the pycnometer measurements since the core is too big to fit into the equipment. In Figure 3-11 the core KA9-L is shown. The arrow in the side of the core indicates the flooding direction. The core end-pieces above and below are the pieces we saved after cutting the oversized core into smaller pieces. Figure 3-12 shows the KA9-L core after cutting it into six smaller parts.

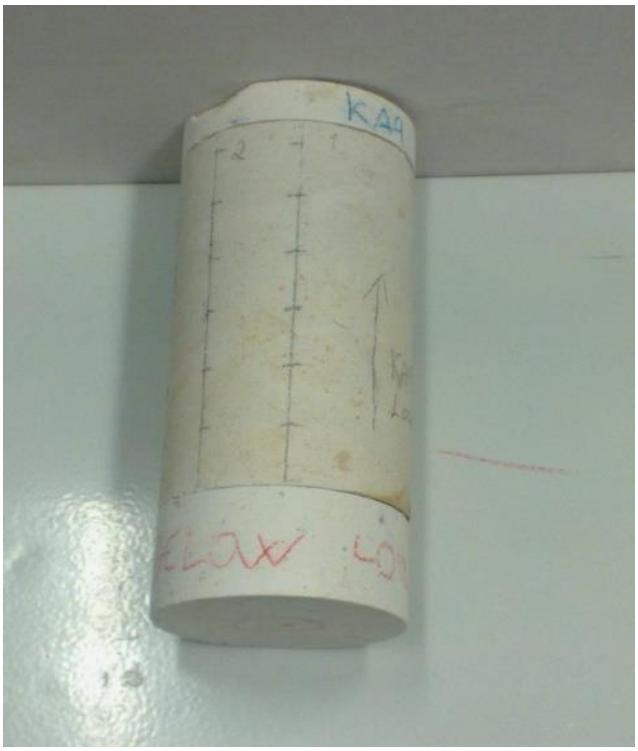

Figure 3-11: The KA9-L core after flooding, with the two unflooded pieces above and below

Figure 3-12: The KA9-L core after cutting and ready for pycnometer measurements

3.4. Flooding Fluids

Two brines were prepared: Sodium chloride (NaCl) and synthetic sea water (SSW). Each flooding fluid was prepared by mixing the salts one by one into 1 liter of distilled water (DW) and stirred for minimum one hour with a magnet stirrer to ensure proper dissolution of all salts. After complete mixing, the solution was filtered with a 0.65 µm pore sixe filter. The pH of the solution was measured with a SevenEasy METTLER TOLEDO pH-meter (Figure 3-13).

Figure 3-13: SevenEasy METTLER TOLEDO pH-meter

The composition of the brines and the concentration of each ion are presented in Table 3-1 and Table 3-2.

	NaCl		SSW	
Salts	g/l	mole/l	g/l	mole/l
NaCl	64.91	1.11	23.38	0.400
KCl			0.75	0.010
$MgCl_2 \cdot 6H_2O$			9.05	0.045
$CaCl_2 \cdot 2H_2O$			1.91	0.013
Na_2SO_4			3.41	0.024
$NaHCO_3$			0.17	0.002

Table 3-1: The composition of the flooding fluids NaCl and SSW

Ions in SSW	Concentration [mole/l]
Cl^-	0.526
SO_4^{2-}	0.024
HCO_3^-	0.002
Na^+	0.450
K^+	0.010
Mg^{2+}	0.045
Ca^{2+}	0.013

Table 3-2: The concentration of ions in SSW.

Carbonated sea water has also been used as flooding fluid. Synthetic sea water with the same composition and ion concentrations in Table 3-1 and Table 3-2 was saturated with CO_2 in a pressure vessel. A given amount (in ml) of liquid CO2 was

flooded into the cell at 70 bar. The density of CO_2 at different pressure and temperature conditions was obtained from the on-line calculator (http://www.peacesoftware.de/einigewerte/co2_e.html).

3.5. Experimental Procedure

Experiments on three long-term tests have been analyzed. The total experimental time was 249, 109 and 203 days for the tests KA9-L, KA24-L and KA28-U, respectively.

The cores were sealed with a plastic shrinking sleeve to avoid leakage of the confining oil and pore fluid. The plastic sleeve was then heated with an industrial heating device to properly attach it to the core. The core with the shrinking sleeve around was placed in the center of the triaxial cell and a steel cylinder was mounted around the core and filled with confining oil (Marcol oil). The cell was sealed with bolts after placing a heating jacket around the cylinder. In order to measure the axial deformation, a LVDT was mounted on top of the cell.

There are some differences in how the three experiments have been performed. Initially, all tests were flooded with approx. 2 pore volumes of distilled water at 1.2 MPa confining stress and 0.7 MPa pore pressure. Then NaCl was introduced to the plug before the temperature was increased from ambient conditions. All tests were performed at uni-axial strain conditions in which the side stresses (confining pressure) was changed in response to the measurements of the circumferential diameter from the extensometer – when the diameter increases/decreases then a Labview routine responds by increasing/decreasing the

confining pressure. A second labview script adjusts the piston pressure to ensure a stable overburden stresses.

In this thesis two types of tests are analyzed. KA9-L and KA24-L were performed at constant pore pressures (0.7 MPa) and the overburden weight was increased by automatic variation in both confining and piston pressure. In these two tests the pore pressure was controlled by a back pressure regulator that allows for continuous collection of effluent samples. After the initial temperature buildup the "depletion phase" is performed by increasing the piston pressure at uni-axial strain conditions (increasing confining pressure) to an overburden stress of 27.7 MPa. During this loading stress-strain curves provide elastic and plastic parameters. After the loading to 27.7 MPa the overburden stress is kept constant. The observed deformation at constant conditions is termed creep. In the KA9-L test we flooded with NaCl brine until a strain rate of 10^{-3} %/hour was obtained and we started a "re-pressurization phase" by reducing the overburden stress to 11.7 MPa. The reduction in overburden stress was performed after 30 days. At 37 days sea water was injected through the plug in the re-pressurized phase and at 149 days flooding with carbonated sea water was initiated. In the KA24-L test sea water and CO_2 was introduced at high axial differential stresses without any re-pressurization after 62 days.

KA28-U was performed in a different manner. Here, the overburden stress was kept constant at all times at 42.7 MPa and the initial yielding phase was performed by reducing the pore pressure from 38.0 MPa to 15 MPa before creep at 27.7 MPa (=42.7-15.0 MPa) axial differential stresses was initiated. This is a test performed at in-situ conditions in which the stress level, pore pressure and temperature conditions are close to those found in real reservoirs. In this case effluent sampling was not possible since the fluids are collected in a closed piston cell in

which the pore pressure is controlled by a pore pressure pump (Teledyne Isco Syringe Pump Model 260D). At 48 days sea water was injected and at 119 days flooding with carbonated water was initiated. The concentration of CO_2 in sea water was changed during this test. After flooding with 3 g/l for two weeks, the concentration of CO_2 was increased to 10 g/l and to 30 g/l after 35 more days.

All tests were flooded with distilled water for 1-4 days at the end of the experiments.

In this thesis the word “depletion” refers to an increase in the axial differential stress. This can be performed either by (a) increasing the axial stress at constant pore pressure (KA9-L and KA24-L), or (b) constant axial stress and reduction in pore pressure (KA28-U). The word “re-pressurization” is associated with the opposite of depletion. For KA9-L re-pressurization is simulated by a reduction in the overburden stress (constant pore pressure), while in a reservoir or a test performed at in-situ conditions re-pressurization is associated with that the pore pressure is increased (at constant axial stress). Re-pressurization has not been performed either for KA24-L or KA28-U.

3.6. Chemical Analysis

Collected water samples during the experiments were analyzed with the Dionex ICS-3000 Ion Chromatography (Figure 3-13). The machine measures the cations and anions separately. Prior to the chemical analysis, the effluent samples had to be diluted 500 times with a Gilson Syringe Pump, Model 402 (Figure 3-14). Each diluted sample was then filtered and 1.5 ml of the sample in the syringe was placed in a small glass suitable for the ionic chromatography machine. Standards from the original flooding fluids were also prepared by the same procedure. Then the ionic chromatography glasses with the effluent and the standards were placed inside the ionic chromatography machine for measurements of the cations and anions.

Figure 3-14: The Dionex ICS-3000 Ion Chromatography

Figure 3-15: Gilson Syringe Pump, Model 402.

The ionic chromatography machine is equipped with a computer that permits precise estimation of peak areas. The peak area for an ion in the effluent are compared with the peak area of the same ion in the standards. Several standards from each flooding fluid are prepared and analyzed in the machine. When comparing the effluent with the standards, we use the average of all the standards. It is important to have good repeatability of the standards. By repeatability, we mean that the peak areas in all the standards for each specific ion should be close to equal. Significant variations in the peak areas in the standards are an indication of error.

From the peak area, we are able to calculate the concentration of each ion in the effluent from the following equation:

$$C_{sample} = \frac{A_{sample} C_{std}}{A_{std}} \qquad \text{(Eq. 3-1)}$$

Where C_{sample} is the ionic concentration in the effluent sample, C_{std} is the average ionic concentration in the standards, A_{sample} is the peak area of the ion in the effluent sample and A_{std} is the average peak area of the ion in the standards.

Comparing the concentration of an ion in the effluent with the concentration of the same ion in the standards tells us if the ionic concentration of the flooding fluid has increased or decreased after flooding through the core. We can estimate the mass change of the plug at a given time from the ionic concentrations:

$$m = C * Q * Mm \qquad \text{(Eq. 3-2)}$$

Where m is the mass of an ion [g], C is the ion concentration [mole/l], Q is the flux [l] and Mm is the molecular mass [g/mole]. The flux Q can be calculated from the following equation:

$$Q = v * t \qquad \text{(Eq. 3-3)}$$

Where v is the flooding rate [l/min] and t is the time [min].

The accumulated mass can then be expressed as:

$$m_{acc} = m_{inj} - m_{prod} \qquad \text{(Eq- 3-4)}$$

Where m_{acc} is the accumulated mass, m_{inj} is the injected mass and m_{prod} is the produced mass. A negative value of the accumulated mass means that we produce more of an ion than what we have injected. Thus, the mass of the core is decreasing. Opposite, a positive value of the accumulated mass is interpreted as an increase of the

core weight because we produce less of an ion than what we injected. The weight of the core at a given time during the test can be estimated by:

$$m_{solid}(t) = m_{solid,0} + \sum_{i=ion} m_{acc,i} \quad \text{(Eq. 3-5)}$$

Where $m_{solid}(t)$ is the solid mass at time (t), $m_{solid,0}$ is the initial weight of the chalk core, and $\Sigma m_{acc,i}$ is the sum of the accumulated mass for all ions.

The charge balance of anions and cations present in the effluent sample can be calculated by:

$$\sum_{i=ion} n_i[C_{a,i}] = \sum_{i=ion} m_i[C_{c,i}] \quad \text{(Eq. 3-6)}$$

Where C_a is the ion concentration of an anion, n is the magnitude of the positive charge of the anion, C_c is the ion concentration of a cation and m is the magnitude of negative charge of the cation.

4. RESULTS

4.1. Mechanical Testing

Three different tests in a triaxial cell under uniaxial strain conditions have been analyzed throughout this project in attempt to answer the questions: What will the injection of CO_2 dissolved in sea water do the geo-mechanical parameters that describe the creep curve, and how will it affect the fluid-rock interactions across the chalk surface? To simplify the comparison between the tests we have used core samples from the same block of outcrop Kansas chalk.

There are some differences in how the three experiments have been performed (see chapter 3.5) and how long the tests have been running. An overview of flooding fluids in each test and the amount of days flooded with each fluid are summarized into Table 4-1.

Test name	Days of flooding						Total test days
	NaCl	SSW	SSW+CO_2			DW	
			3 g/l	10 g/l	30 g/l		
KA9-L	37	23	84	-	-	3	249
KA24-L	58	-	47	-	-	1	109
KA28-U	48	71	14	35	31	4	203

Table 4-1: Overview of flooding with different fluids in KA9-L, KA24-L and KA28-U. The composition of the pore fluids are shown in Table 3-1.

4.1.1. MEASUREMENTS BEFORE FLOODING

Different properties of the chalk core were measured and calculated before flooding. These properties are presented in Table 4-2. Porosity, bulk volume, pore volume and density are calculated from Eq. 2-29, Eq. 2-30, Eq. 2-31 and Eq. 2-32, respectively.

Test Name	Length L [mm]	Diameter D [mm]	Wet Weight W_W [g]	Dry Weight W_D [g]	Bulk Volume V_B [mL]	Pore Volume V_P [mL]	Porosity ϕ [%]	Density ρ [g/ml]
KA9-L	70,55	37.05	154.96	125.57	76.06	29.39	38.64	2.72
KA24-L	74.40	37.00	168.42	140.06	79.91	28.36	35.49	2.71
KA28-U	73.93	37.99	170.80	138.10	83.80	32.70	39.02	2.72

Table 4-2: Properties of the core before flooding.

4.1.2. YIELD ANALYSIS

All cores were flooded with 1.1 M NaCl during the yield phase. KA24-L also has three days of flooding with DW before NaCl flooding was initiated. But the elastic parameters are estimated from the part of the curve were the core is flooded with NaCl.

The stress level was increased gradually to reach the desired axial stress value. The axial deformation was logged continuously by Labview software program. The axial differential stress is used in the curves. Not subtracting the pore pressure from the axial stress will give a higher yield value because the pore pressure inside the core strengthens the material.

4.1.2.1. Stress-Strain Relationship

Figure 4-1, Figure 4-2 and Figure 4-3 show the axial differential stress plotted as a function of axial strain for the tests KA9-L, KA24-L and KA28-U, respectively.

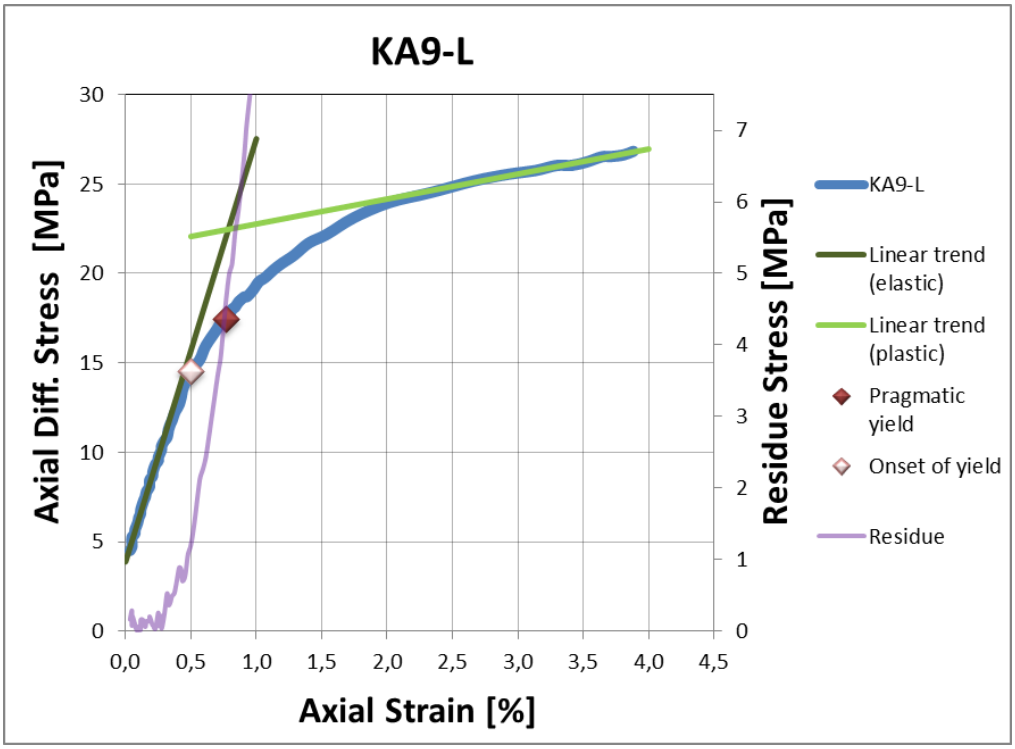

Figure 4-1: The axial stress-strain relationship for KA9-L

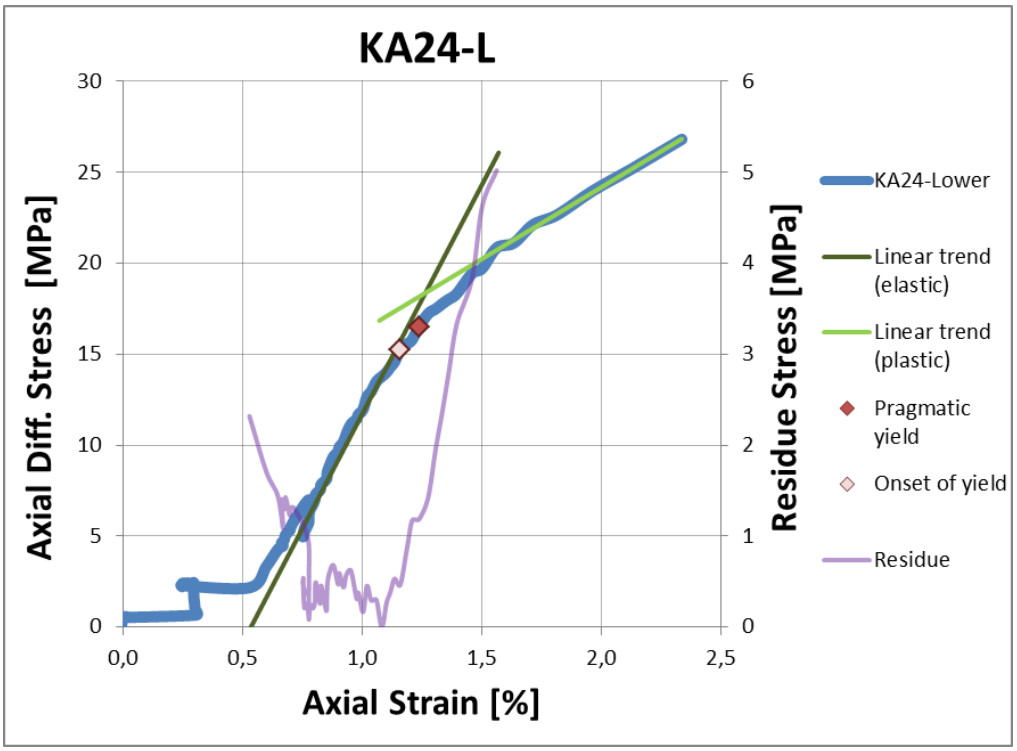

Figure 4-2: The axial stress-strain relationship for KA24-L

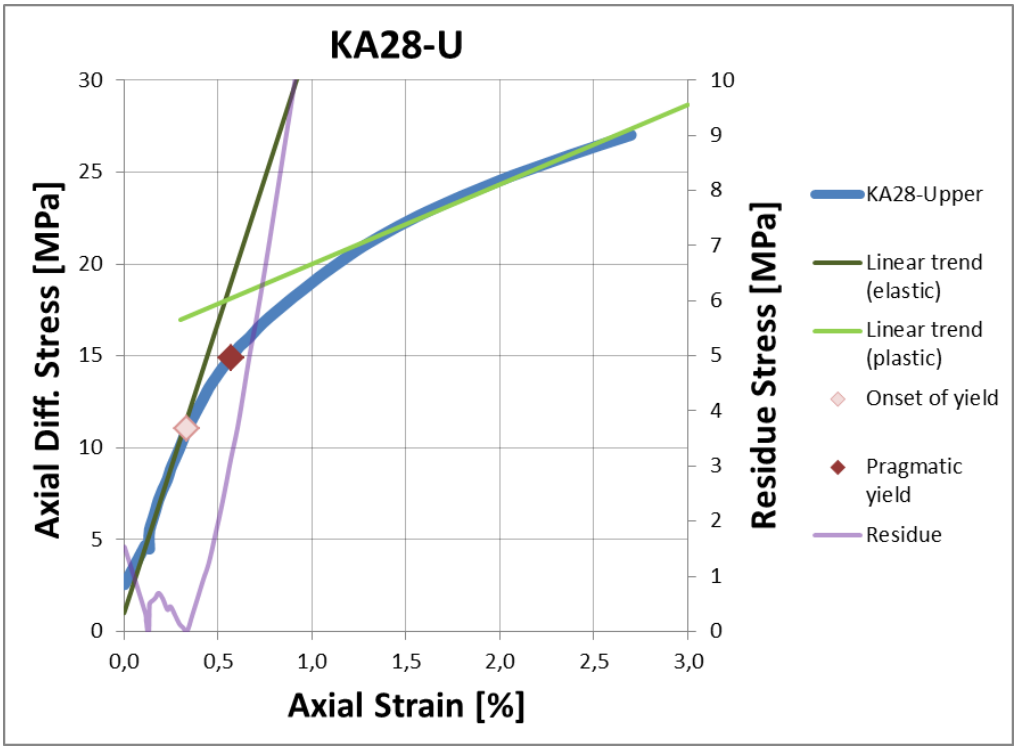

Figure 4-3: The axial stress-strain relationship for KA28-U in which the overburden was kept constant at 42.5 MPa and the pore pressure was reduced to 15 MPa.

The curves are linear at the beginning of the test before it starts to deviate. This is the point representing the onset of yield. As the curve deviates even more from the linear trend we reach the pragmatic yield where the elastic and plastic strain curve has the same stress value. The deviation is easier to observe by plotting the *residue*:

$$R = \sqrt{(a-b)^2} \qquad \text{(Eq. 4-1)}$$

Where R is the residue, a is the stress value in one strain level and b is the linear line value of the elastic regime in the same strain level. The residual is zero if the stress-strain curve and the linear line of the elastic region match completely. Deviation from the linear trend is observed by an increasing residual value.

The mechanical properties onset of yield, pragmatic yield, E-modulus and axial strain for the three tests are listed in Table 4-3.

Test name	Onset of yield [MPa]	Pragmatic yield [MPa]	E-modulus [GPa]	Axial strain [%]
KA9-L	14.5	17.4	2,3	3.8
KA24-L	15.2	16.5	2.2	2.1
KA28-U	11.0	14.9	2.8	2.7

Table 4-3: Mechanical properties of the three test cores.

4.1.3. CREEP ANALYSIS

When the differential axial stress equals the pre-set level and is constant, the creep phase starts. The material are now exposed to axial differential stresses fare into the plastic region were deformation is irreversible.

In the beginning of the creep phase all of the tests cores were flooded with NaCl, followed by SSW flooding for KA9-L and KA28-U in 112 and 71 days respectively. The test KA24-L was not flooded with SSW alone. The injection of sea water carbonated with 3g/l CO_2 was initiated after 149, 58 and 116 creep days in KA9-L, KA24-L and KA28-U, respectively. The concentration of CO_2 was constant throughout the tests KA9-L and KA24-L. In KA28-U the concentration was increased to 10 g/l after 134 creep days and further increased to 30g/l after 169 creep days. At the end of the tests the cores were flooded with DW for 1-4 days.

KA9-L went through a re-pressurization phase after 30 days of creep and reaching a creep rate of 10^{-3} %/hr. The overburden stress was reduced from 27.7 to 11.7 MPa.

4.1.3.1. Axial Creep Strain vs. Creep Time

Plotting the axial creep strain as a function of creep time, enable us to observe the deformation of the core over time, which is demonstrated in Figure 4-4, Figure 4-5 and Figure 4-6. The statistical parameterization of Power law (See chapter 2.6.4) is fitted to the observed creep strain curve, where the appropriate values for A and b are adjusted for each flooding fluid. The square time dependency model has been applied to fit the area of the creep curve for KA28-U where accelerating creep is experienced. The residue represents the difference between the observed axial creep strain and the

power low fit. The residue value is close to zero when there is a good match between the creep curve and the power law adjustment.

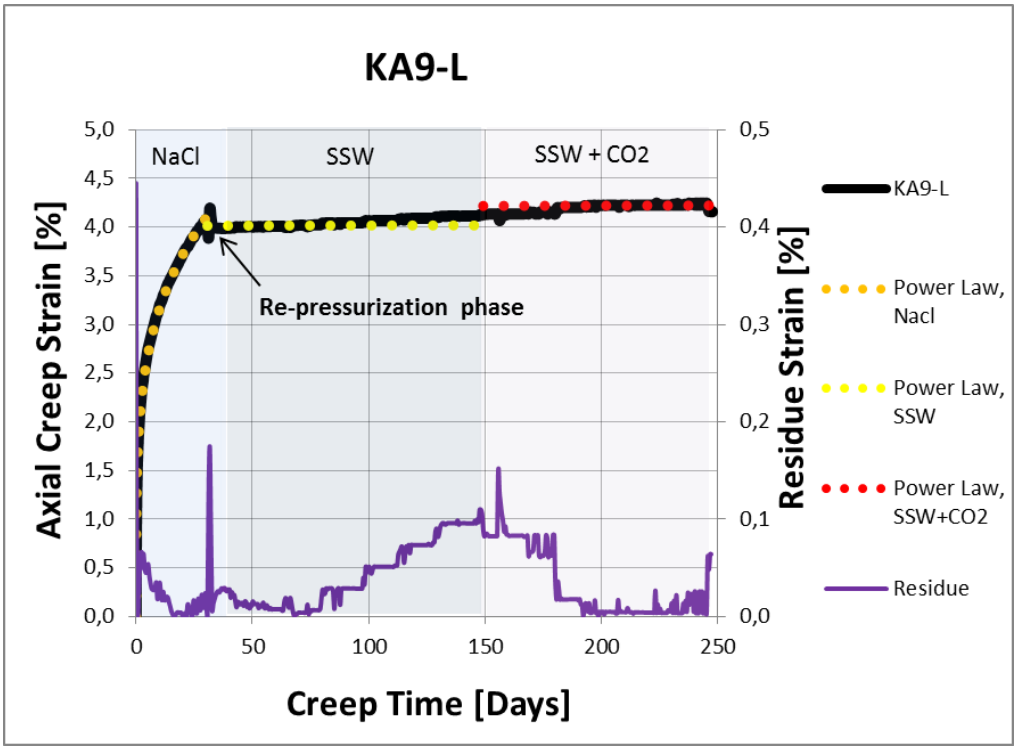

Figure 4-4: The observed creep curve through time at the uniaxial strain condition for KA9-L, where the best fit of power law to the observed creep strain curve is represented by the scatter lines

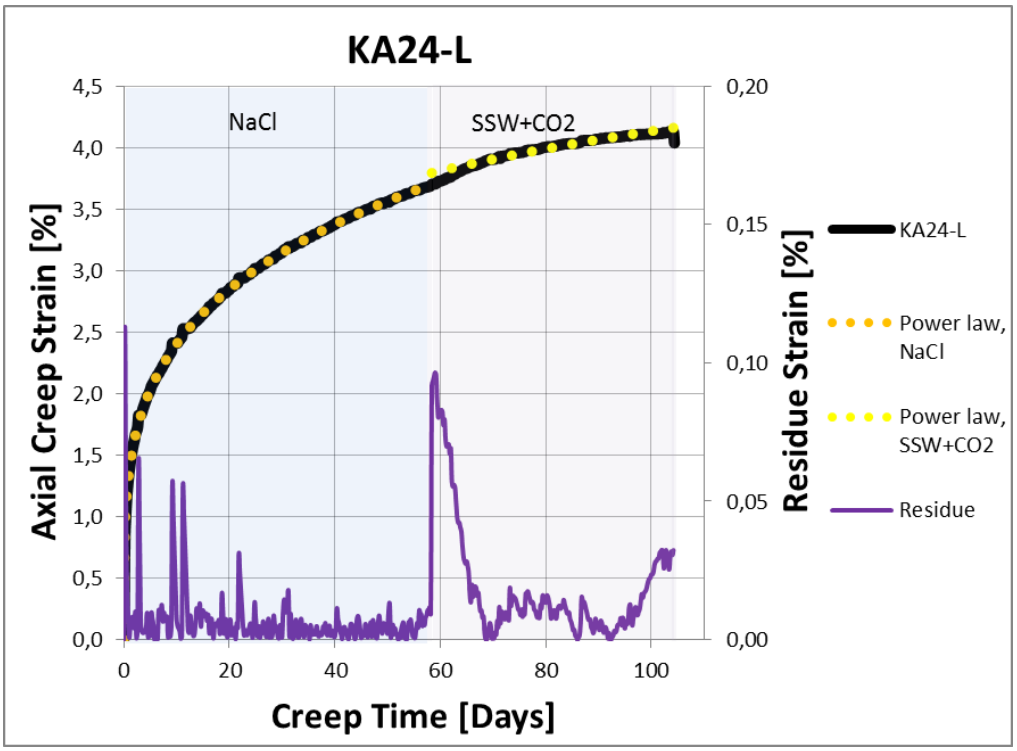

Figure 4-5: The observed creep curve through tine a uniaxial strain conditions for KA24-L, where the best fit of power law to the observed creep strain curve is represented by the scatter line

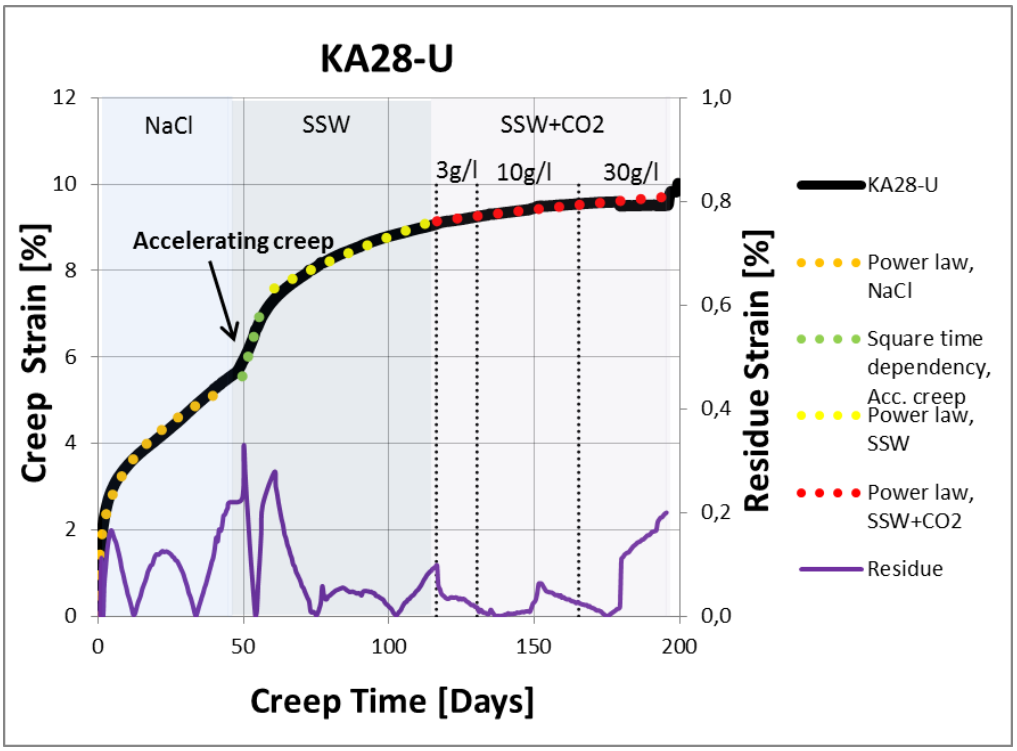

Figure 4-6: The observed creep curve through tine a uniaxial strain conditions for KA28-U, where the best fit of power law to the observed creep strain curve is represented by the scatter line

The values for A and B in Power at various stages of the creep in each test curve with different flooding fluids are given in Table 4-4.

Test name	Flooding Fluid	A	B
KA9-L	NaCl	0.86	0.24
	SSW	3.99	$5.93 \cdot 10^{-4}$
	SSW+CO_2	4.15	$2.06 \cdot 10^{-3}$
KA24-L	NaCl	0.63	0.25
	SSW+CO_2	1.20	0.16
KA28-U	NaCl	0.73	0.28
	SSW	0.92	0.29
	SSW+CO_2	3.66	0.12

Table 4-4: Values for the parameters A and B in Power law.

The axial creep strain at the end of the flooding periods for each fluid, as well as the total axial strain throughout the entire test is given in Table 4-5.

Test name	Axial creep strain [%]						Total axial strain [%]
	NaCl	SSW	SSW+CO_2			DW	
			3 g/l	10 g/l	30 g/l		
KA9-L	3.9	4.1	4.2	-	-	4.1	7.9
KA24-L	3.7	-	4.1	-	-	3.9	6,0
KA28-U	5.5	9,0	9.2	9.5	9.5	10.1	12.8

Table 4-5: The axial creep strain at the end of each flooding period with a fluid and the total axial strain obtained from KA9-L, KA26-L and KA28-U.

4.1.3.2. Creep Strain Rate vs. Creep Time

The creep strain rate in %/hour is plotted as a function of creep time for all three tests in Figure 4-7. We can see from the plot that the strain rate is higher in the beginning and decreases over time. Except from the KA28-U test where the strain rate is increases when sea water flooding is initiated and at the end of the test when the core is flooded with distilled water. The strain rate also starts to increase when flooding KA9-L with DW at the end.

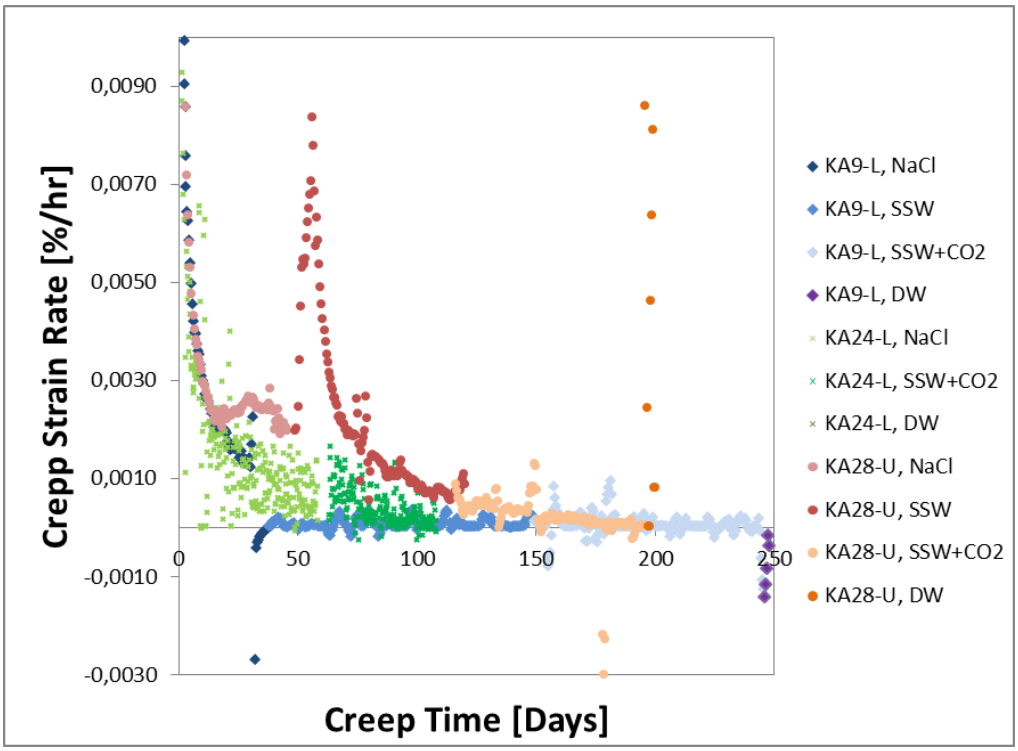

Figure 4-7: Creep stain rate versus creep time for KA-9L, KA24-L and KA28-U.

4.1.3.3. Pressure Development Trough Time

There are several different types of pressure in our tests. Some of them are held constant through the experiment, while others are varied. The confining pressure (p_{conf}), piston pressure (p_{piston}), pore pressure (p_{pore}) and axial differentil stress is plotted as a function of creep time together with the creep curve in Figure 4-8, Figure 4-9 and Figure 4-10 to illustrate how the they are related to one another.

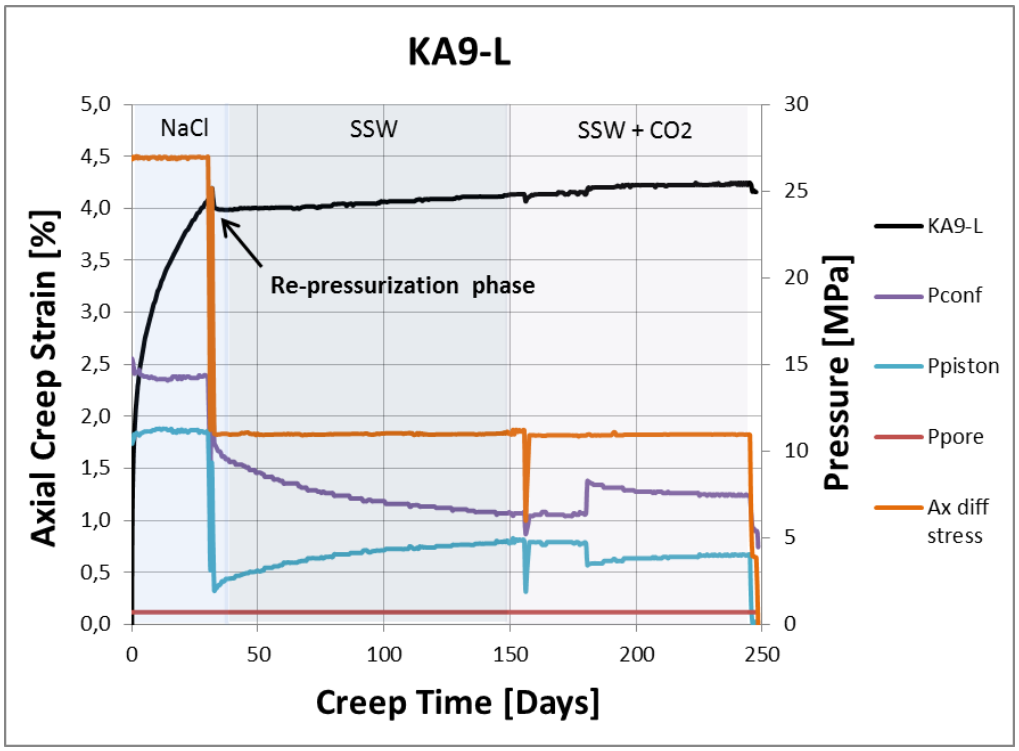

Figure 4-8: Different types of pressure in KA9-L plotted as a function of creep time together with the creep curve.

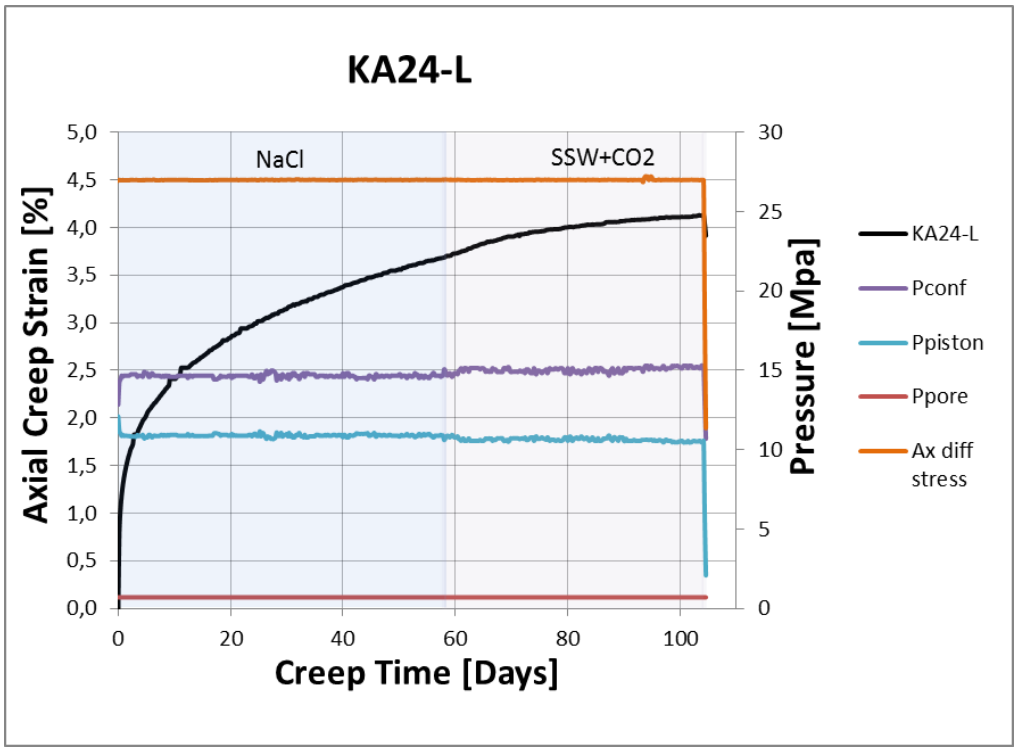

Figure 4-9: Different types of pressure in KA24-L plotted as a function of creep time together with the creep curve. Here we see how the confining pressure increases slightly when sea water is introduced to the plug, meaning that the plug require higher support from the confining pressure to maintain its radial diameter. This indicates that the plug is weakened.

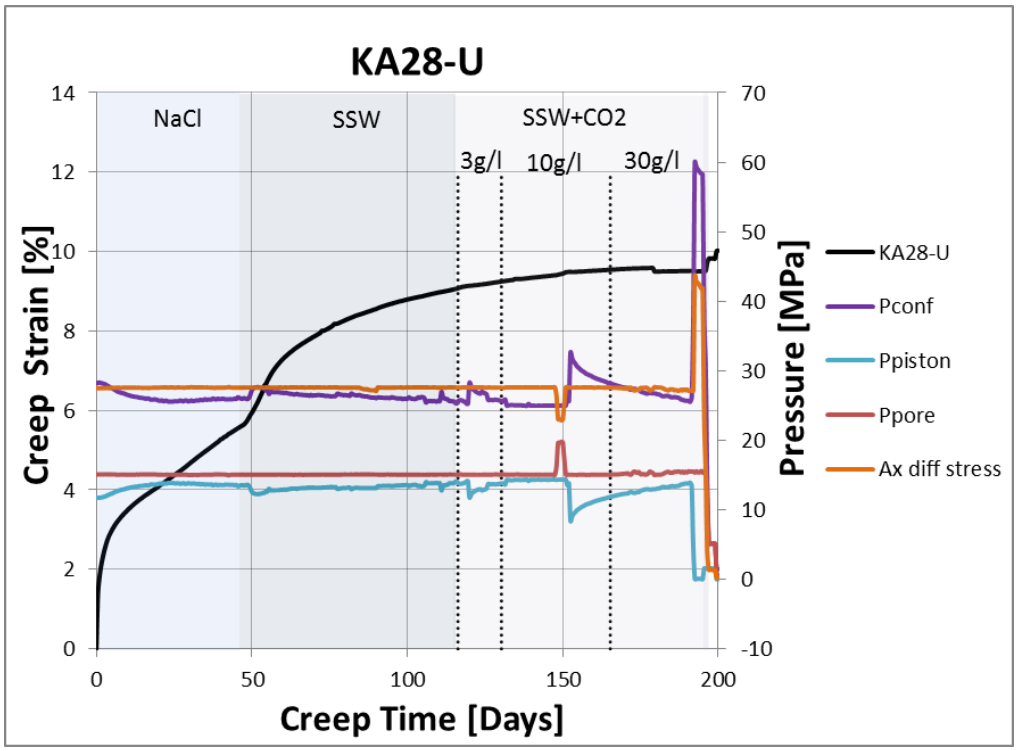

Figure 4-10: Different types of pressure in KA28-U plotted as a function of creep time together with the creep curve.

4.1.3.4. Permeability Development Through Time

The permeability is calculated from Darcy`s law (see chapter 2.6.5). The permeability variations in our experiments are high, because the differential pressure instabilities are significant. The permeability and differential pressure as a function of creep time is plotted in Figure 4-11, Figure 4-12 and Figure 4-13 to show how the permeability is related to the differential pressure and how it varies through the testes.

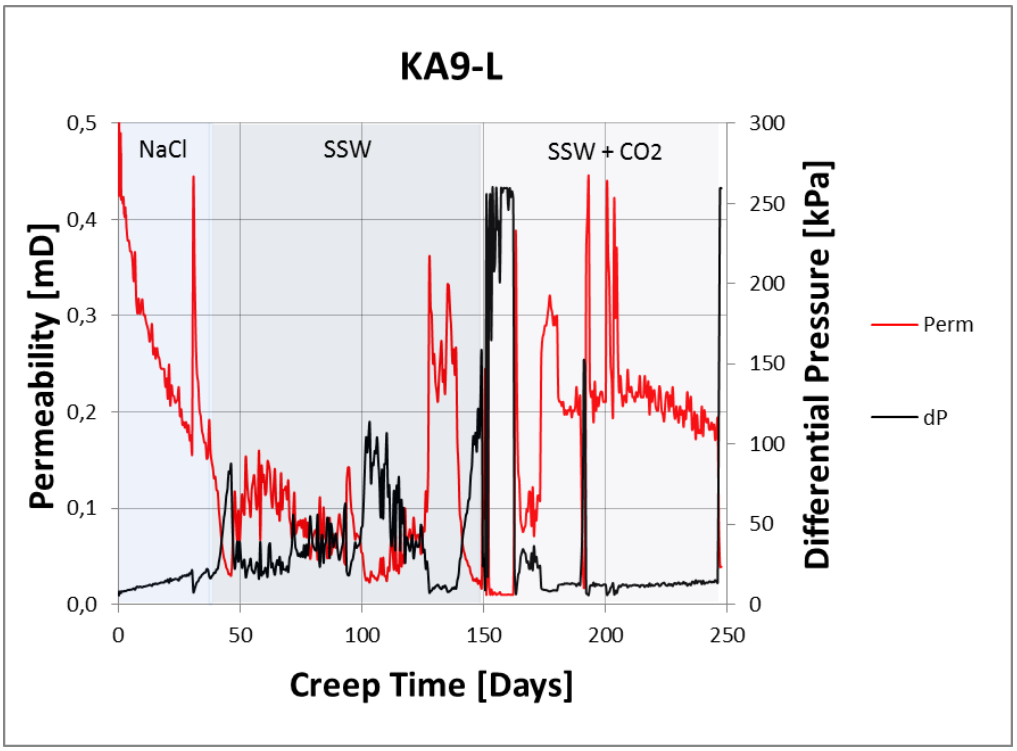

Figure 4-11: Permeability and differential pressure versus creep time for KA9-L

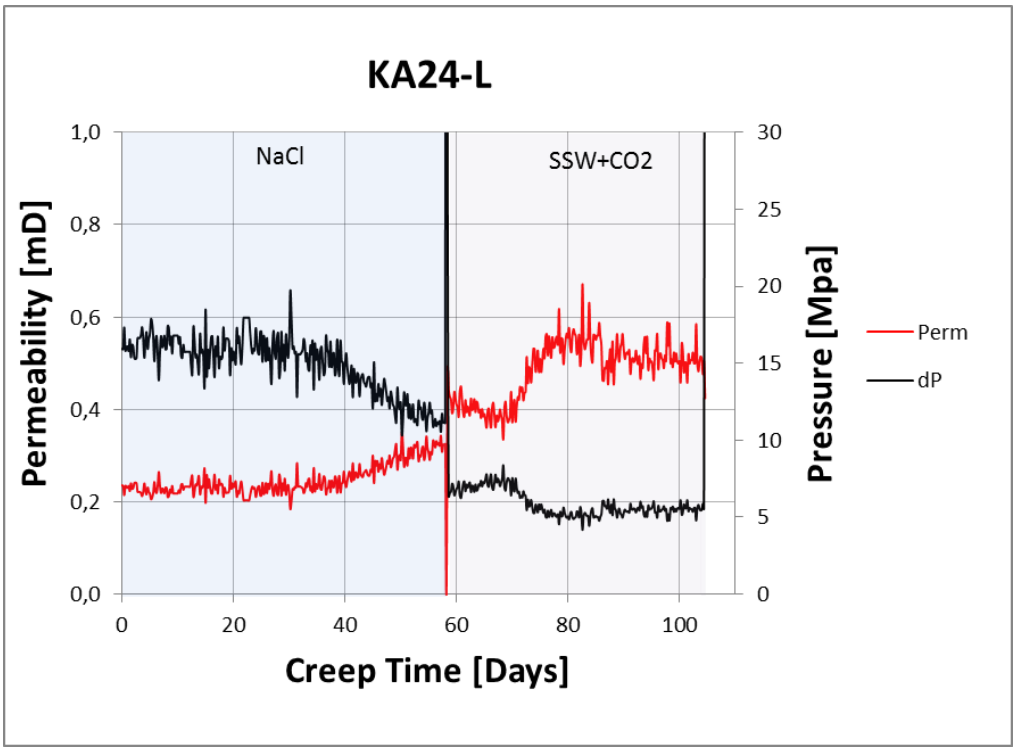

Figure 4-12: Permeability and differential pressure versus creep time for KA24-L.

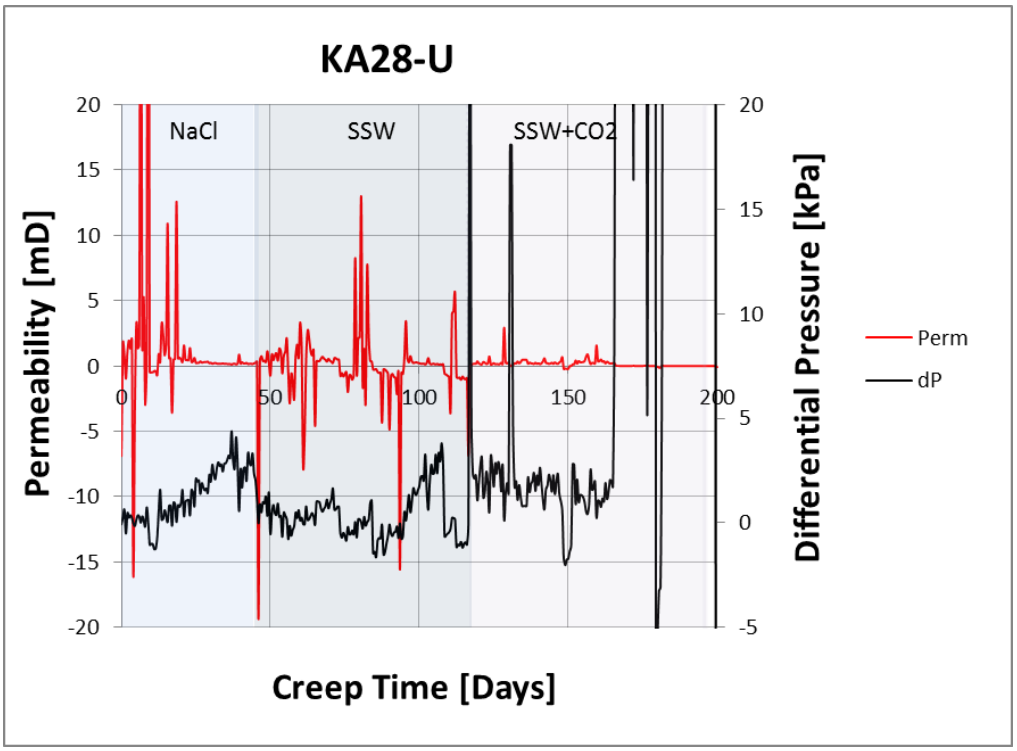

Figure 4-13: Permeability and differential pressure versus creep time for KA28-U.

4.1.4. Q-P' DIAGRAMS

The yield and failure data can be expressed through a q-p'-diagram. Such diagrams for KA9-L, KA24-L and KA28-U are plotted in Figure 4-14, Figure 4-15 and Figure 4-16, respectively. The onset of yield and pragmatic yield are marked in the diagrams to show the boundaries between elastic and plastic phase.

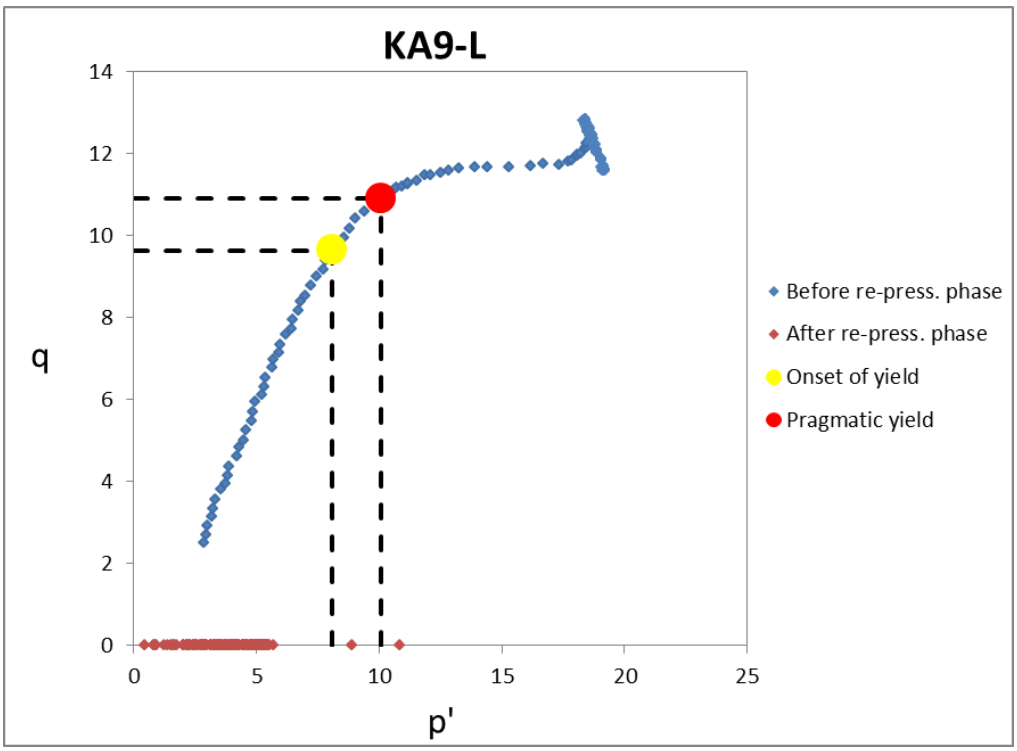

Figure 4-14: q-p' diagram for KA9-L., where q and p' is calculated from the radial and axial stress

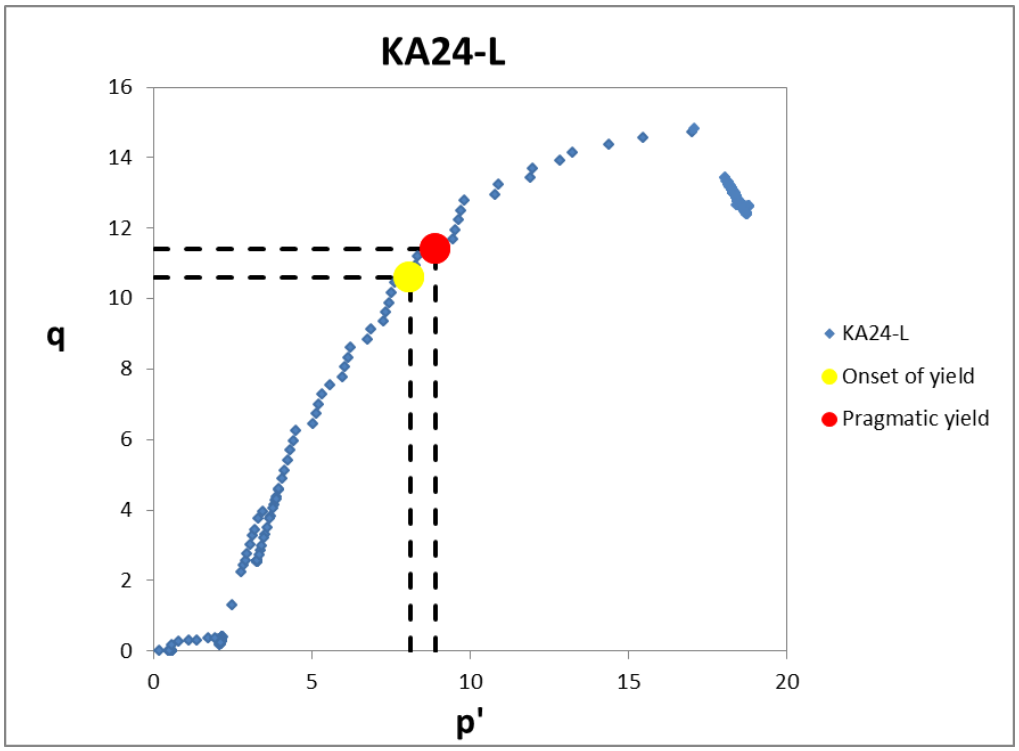

Figure 4-15: q-p' diagram for KA24-L., where q and p' is calculated from the radial and axial stress.

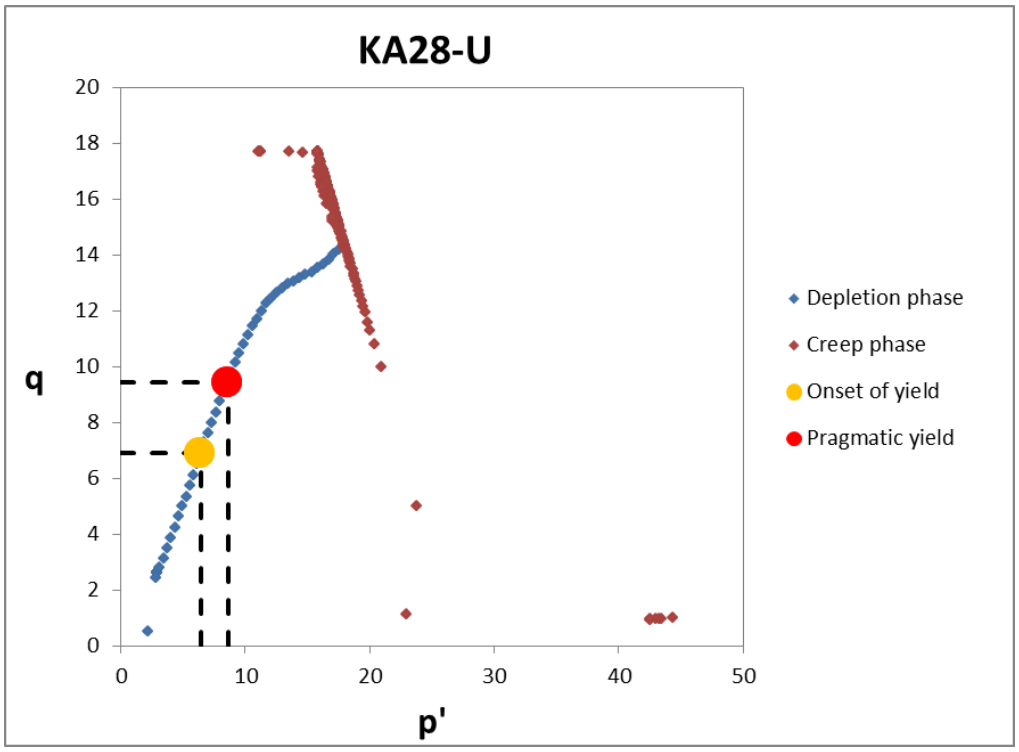

Figure 4-16: q-p' diagram for KA28-U., where q and p' is calculated from the radial and axial stress.

4.1.5. POROSITY DEVELOPMENT

The change in porosity through time is effected by both mechanical and chemical factors. In Figure 4-17 and Figure 4-18 we have plotted the mechanical porosity according to Eq. 2-40, and the total porosity including chemical and mechanical contribution from Eq. 2-42 for the tests KA9-L and KA24-L. The difference between the total porosity and mechanical porosity represents the chemical porosity. The calculations involved to estimate the total porosity includes the mass change. We can estimate the mass change based on our ionic chromatography results from effluent samples collected through the tests. It should be noted that the mass change based on the results from the ionic chromatography analysis did not fit the mass change based on dry weight measurements before and after flooding of the core to a satisfying degree. In order to predict and be able to illustrate the thought behind porosity evolution through time, we did a correction of the time dependent mass change. The correction is based on the difference between total mass change from before and after dry weight measurements of the plug, ΔM_{IC}, and the total mass change calculated from the ionic chromatography results $\Delta M_{Measure}$:

$$M_{corr} = \frac{\Delta M_{IC}}{\Delta M_{Measure}} \qquad \text{(Eq. 4-2)}$$

(Eq. 2-142 also incorporates the change in density through time. We can estimate the initial density of the core before flooding and the density of the plug after flooding by the pycnometer measurements. But we do not have any recording of how the density changes through the rest of the test. Our best estimate is that the density develops linearly through time. Then we can find the density at a given time by the equation for a linear line:

$$\rho_{(t)} = \rho_0 + t\frac{\Delta\rho}{\Delta t} \qquad \text{(Eq. 4-3)}$$

Where $\rho_{(t)}$ is the density at a given time *(t)*, $\rho_{(0)}$ is the initial density before flooding, t is the time and $\Delta\rho/\Delta t$ is the slope of the linear curve.

Hvorfor det ikke går ann å ta vannprøver vedKA28-testen??

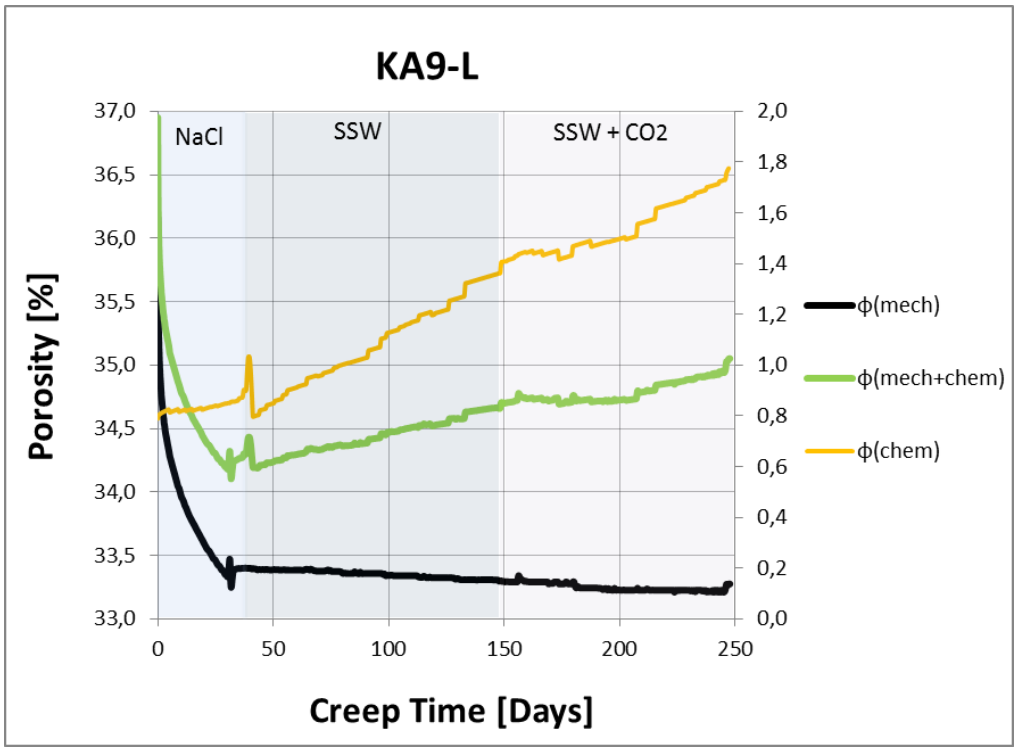

Figure 4-17: Total porosity, mechanical porosity and chemical porosity plotted as a function of creep time for KA9-L

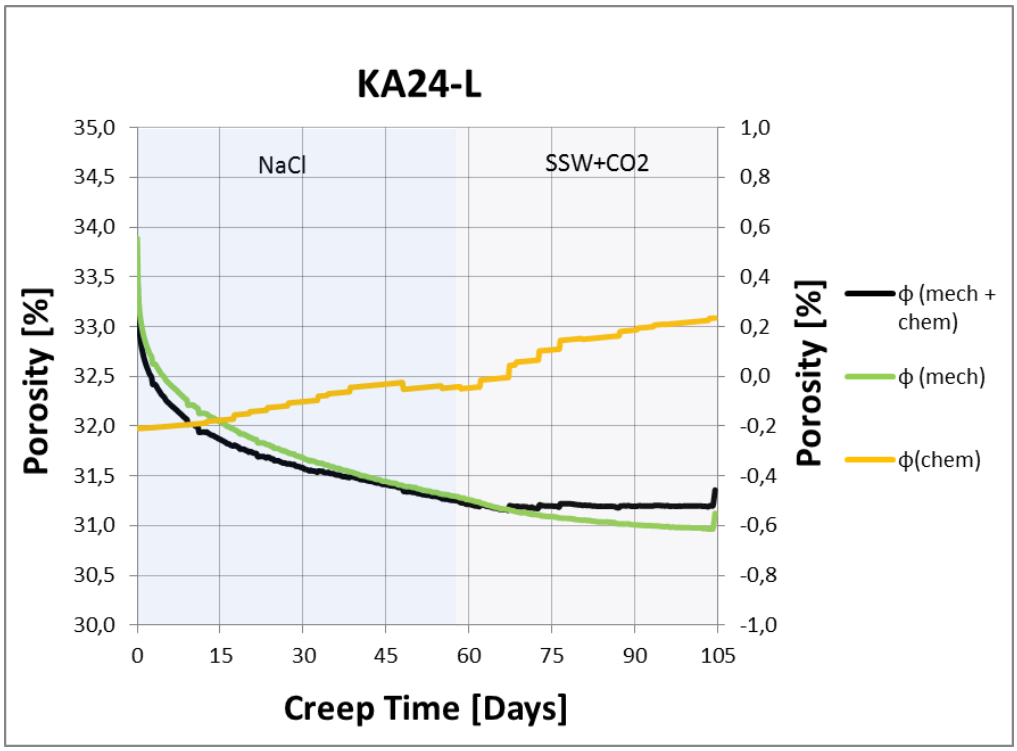

Figure 4-18: Total porosity, mechanical porosity and chemical porosity plotted as a function of creep time for KA24-L.

Collecting effluent samples from KA28-U has not been possible because of the varying pore pressure. Thus, we are not able to plot the development in total porosity over time like for the two other tests, but just the mechanical porosity as shown in Figure 4-19.

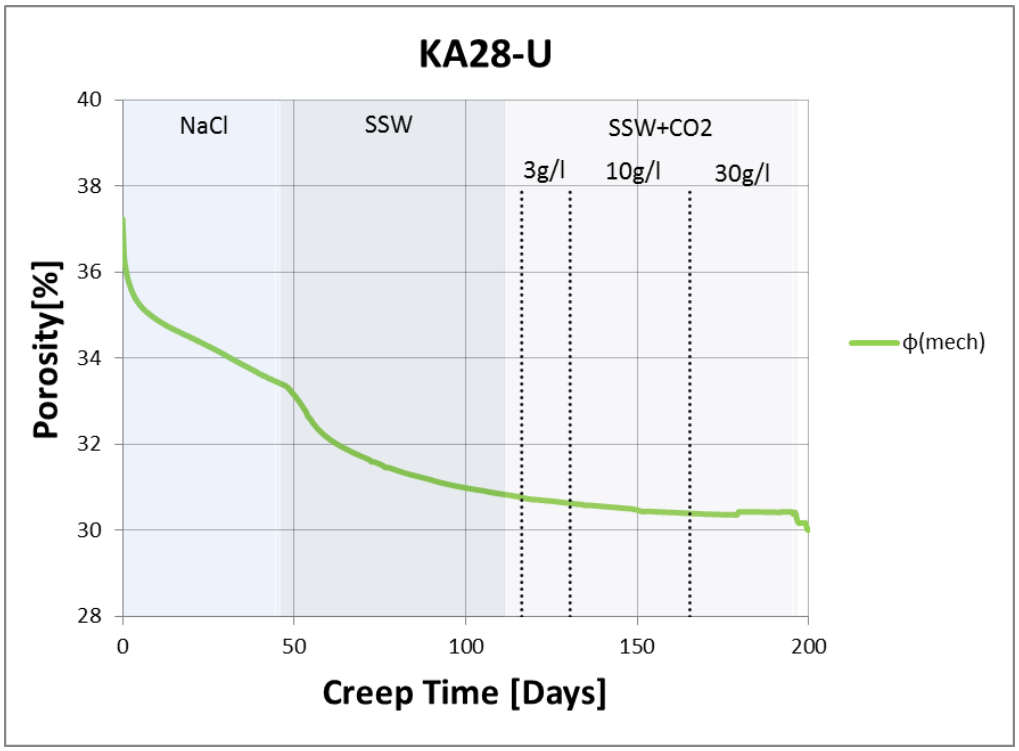

Figure 4-19: Mechanical porosity plotted as a function of creep time for KA28-U.

4.1.6. STRAIN PARTITIONING

The observed strain depends on the mechanical stress level and the chemical induced strain arising from rock-fluid interactions. Figure 4-20 and Figure 4-21 illustrate the strain partitioning for KA9-L and KA24-L, where we divide the observed strain into three curves representing the total observed strain, the chemical strain and the mechanical strain. The total observed strain includes chemical and mechanical contribution to the strain as is logged regularly by the Labview Software. The changes in solid volume by dissolution/precipitation processes, representing the chemical strain, are calculated from Eq. 2-45. The change in mass and change in density is estimated in the same manner as for porosity. Therefore, it should be emphasized also for strain partitioning that we have performed a correction of the mass change and considered the change in density through the tests as a linear

relationship in order to illustrate our thoughts around strain partitioning. Thus, no strain partitioning is conducted for KA28-U where no effluent samples are collected during flooding.

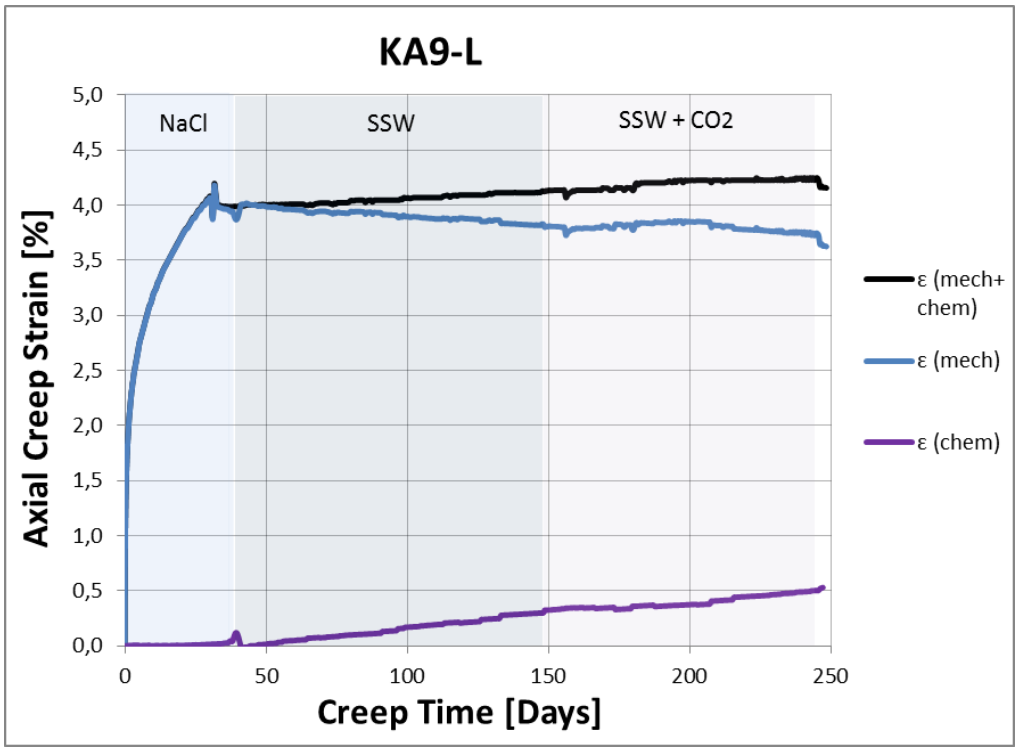

Figure 4-20: Strain partitioning for KA9-L, where total observed strain, mechanical strain and chemical srain is plotted as a function of creep time.

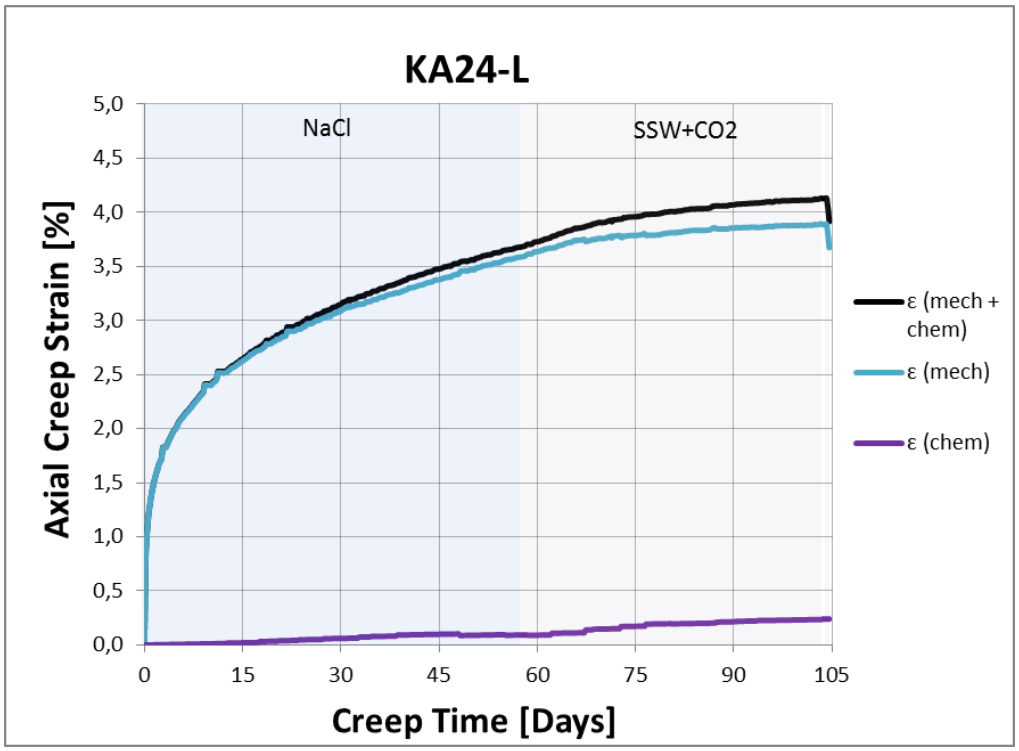

Figure 4-21: Strain partitioning for KA24-L, where total observed strain, mechanical strain and chemical strain is plotted as a function of creep time.

4.1.7. MEASUREMENTS AFTER FLOODING

Properties of the cores were measured and calculated also after flooding. The results are given in Table 4-6. The average value of length, diameter and density is presented. All results from pycnometer measurements with dry weight, solid volume, density and standard deviation for each piece measured is presented in Table 4-7, including pieces not flooded and flooded pieces.

Test Name	Length L [mm]	Diameter D [mm]	Wet Weight W_W [g]	Dry Weight W_D [g]	Bulk Volume V_B [mL]	Pore Volume V_P [mL]	Porosity ϕ [%]	Density ρ [g/ml]
KA9-L	64.62	37.04	148.60	125.01	69.56	23.59	33.91	2.75
KA24-L	70.97	37.05	164.28	139.59	76.51	24.69	32.63	2.72
KA28-U	65.36	37.89	160.69	136.99	73.71	23.70	32.15	2.72

Table 4-6: Properties of the cores after flooding.

Test Name	Piece name	W_D [g]	V_S [cm^3]	Std. deviation [cm^3]	ρ [g/cm^3]
KA9-L Not flooded	Between	31.3	11.52	0.0078	2.716
	Below	13.23	4.85	0.0059	2.730
	Between + Below	44.53	16.34	0.0083	2.725
Average					2.724
KA9-L Flooded	1 (Center piece)	13.51	4.91	0.0029	2.752
	1 (Outer piece)	5.07	1.84	0.0037	2.755
	2	13.48	4,92	0.0032	2.741
	3	9.20	3.34	0.0011	2.757
	4	11.22	4.07	0.0022	2.757
	5	13.06	4.79	0.0019	2.725
	6	10.35	3.73	0.0030	2.773
Average					2.752
KA24-L Not	Below	11.35	4.18	0,0027	2,714
	Between	16.34	6.05	0,0103	2,699

flooded	Above	15.10	5.57	0,0043	2,711
Average					2.708
KA24-L	1	10.07	3.69	0.0012	2.731
Flooded	2	8.64	3.14	0.0038	2.750
	3	5.39	1.99	0.0023	2.712
	4	7.84	2.90	0.0044	2.706
	5	6.79	2.51	0.0059	2.702
	6	8.14	3.00	0.0020	2.712
	7	8.16	3.01	0.0025	2.707
Average					2.717
KA28-U	Below	15.77	5.79	0.0131	2.724
Not	Between	15.78	5.76	0.0111	2.739
flooded	Above	28.66	10.56	0.0057	2.715
Average					2.726
KA28-U	1	8.37	3.09	0.0044	2.713
Flooded	2	8.29	3.06	0.0022	2.710
	3	10.42	3.85	0.0046	2.706
	4	9.08	3.37	0.0032	2.696
	5	9.32	3.41	0.0018	2.731
	6	10.24	3.74	0.0025	2.741
Average					2.716

Table 4-7: Pycnometer measurements, mass measurements and calculated densities for KA9-L, KA24-L and KA9-U.

4.2. Chemical Analysis: Ionic Chromatography

During flooding in KA9-L and KA24-L, effluent samples were collected regularly. 96 effluent samples were collected during the KA9-L test and 28 samples from the KA24-L test. The effluent samples were analyzed through ionic chromatography which enables us to calculate the concentrations of different ions in the samples and compare the concentrations with the original concentration of the specific fluid the core was flooded with. It makes it possible to determine if ions are produced or retained by the core. The concentration of Na^{2+} and Cl^{-} ions in the effluent together with the ionic concentrations of the standards seen as the stippled lines, are shown in Figure 4-22 for KA9-L and in Figure 4-23 for KA24-L.

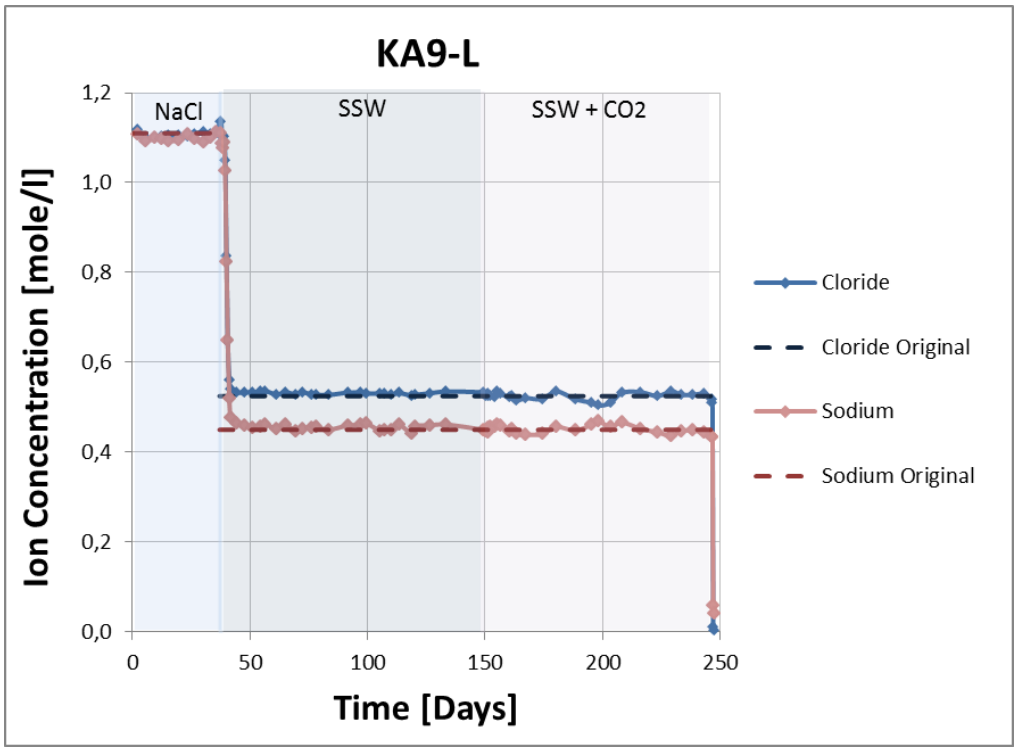

Figure 4-22: The concentration of Na^{+} and Cl^{-} ions in the effluent samples and in the standard for KA9-L.

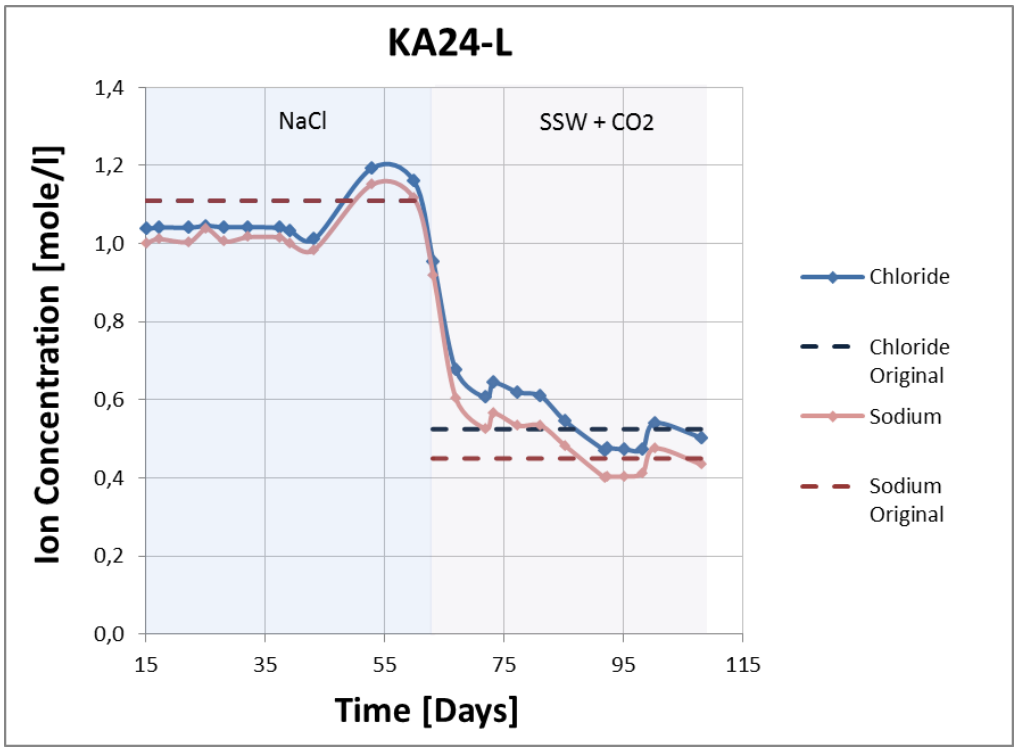

Figure 4-23: The concentration of Na^+ and Cl^- ions in the effluent samples and in the standard for KA24-L.

The concentrations for the other compounds in the effluent and the original concentrations in the standards including HCO_3^-, SO_4^{2-}, Mg^{2+}, Ca^{2+} and K^+ are presented in Figure 4-25 for KA9-L and in Figure 4-26 for KA24-L.

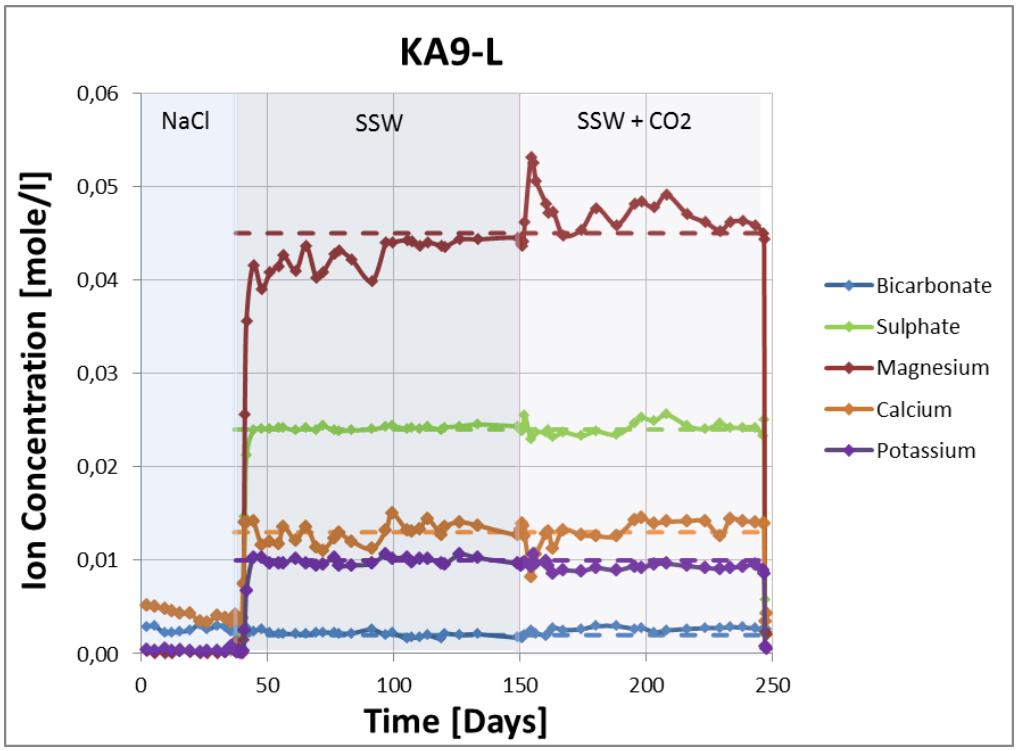

Figure 4-24: The concentration of HCO_3^-, SO_4^{2-}, Mg^{2+}, Ca^{2+} and K^+ ions in the effluent samples and in the standard for KA9-L.

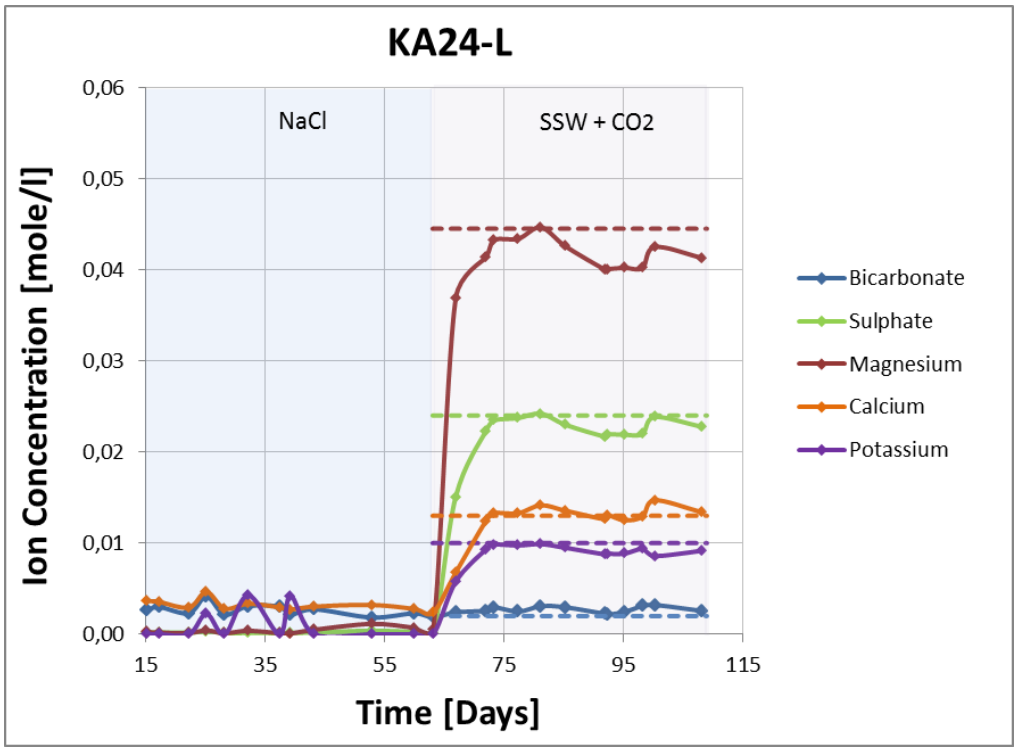

Figure 4-25: The concentration of HCO_3^-, SO_4^{2-}, Mg^{2+}, Ca^{2+} and K^+ ions in the effluent samples and in the standard for KA24-L.

The total mass change is presented in Figure 4-28 for KA9-L and in Figure 4-29 for KA24-L. Note that the mass change is calculated from the injected mass minus the produced mass in the effluent. Thus, a negative value is interpreted as a decrease in plug weight where mass is dissolved, and a positive value is interpreted as an increase in plug weight.

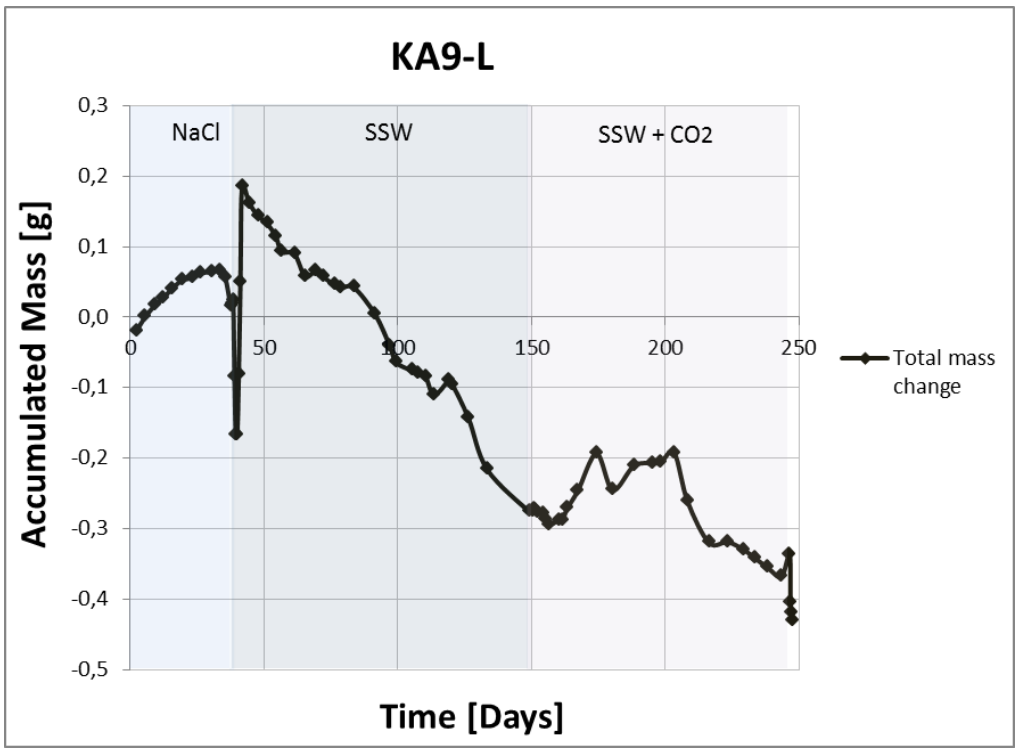

Figure 4-26: The accumulated mass as a function of time for KA9-L

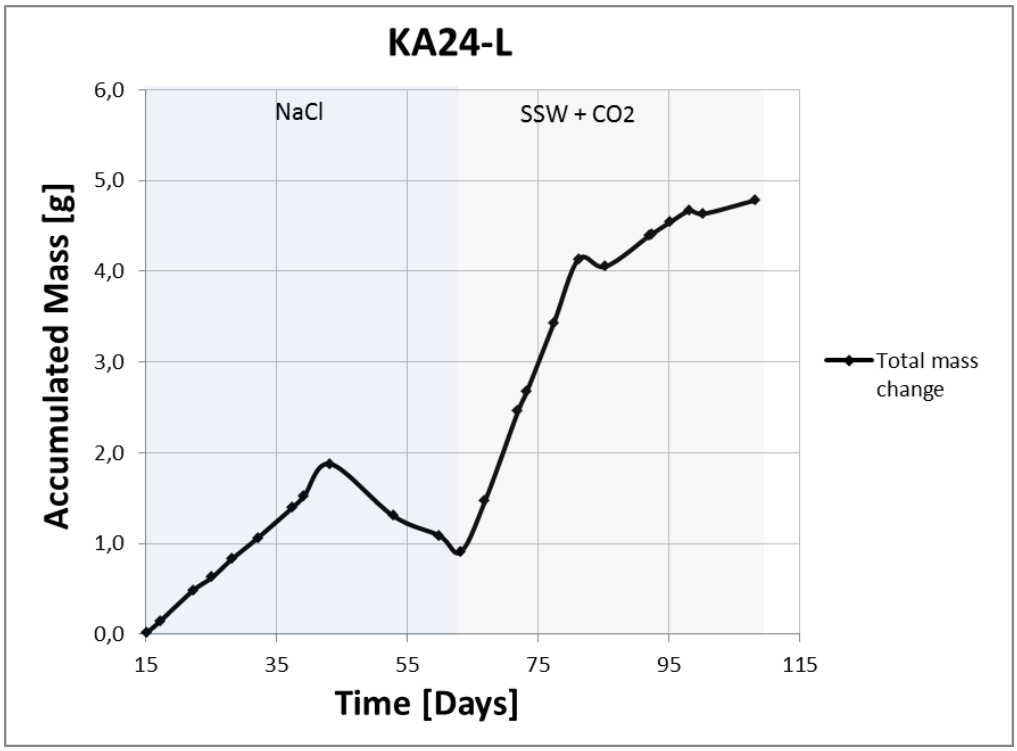

Figure 4-27: The accumulated mass as a function of time for KA24-L.

Figure 4-297 illustrates clearly how big the gap is between the mass change calculated from ionic chromatography test results and the mass change from before and after measurements of the core weight. Possible explanations and errors are presented in the discussion.

The mass change based on ionic chromatography results ΔM_{IC} and from dry weight measurements $\Delta M_{Measure}$, as well as the correction factors M_{corr} used in porosity and strain partitioning calculations are given in Table 4-8.

Test Name	$\Delta M_{Measure}$	ΔM_{IC}	M_{corr}
KA9-L	-0,56	-0,43	1,302
KA24-L	-0,47	4,78	-0,098

Table 4-8: Mass changes and correction factor values for KA9-L and KA24-L

The charge balance is plotted as a function of time in Figure 4-28 for KA9-L and Figure 4-29 for KA24-L to illustrate the balance between negatively charged anions and positively charged cations.

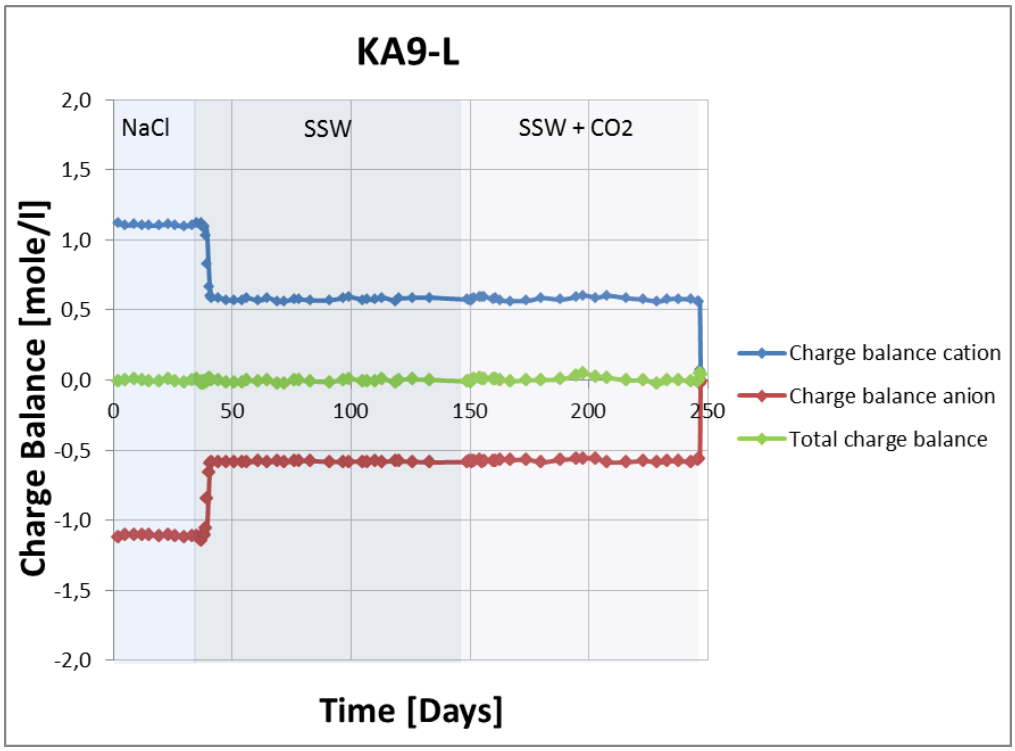

Figure 4-28: The charge balance of cations and anions in the effluent samples in KA9-L test.

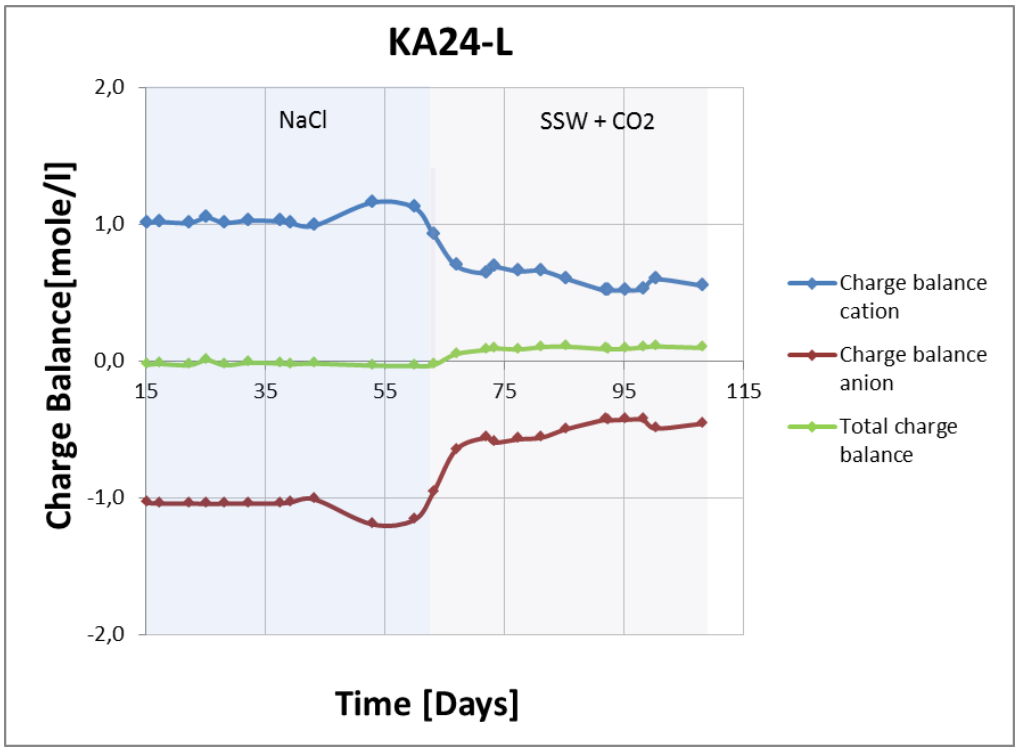

Figure 4-29: The charge balance between cations and anions in the effluent samples for the KA24-L test.

The pH in most of the effluents was measured. The result for KA9-L and KA24-L is presented in Figure 4-30. The pH of the standards is represented by the dotted lines.

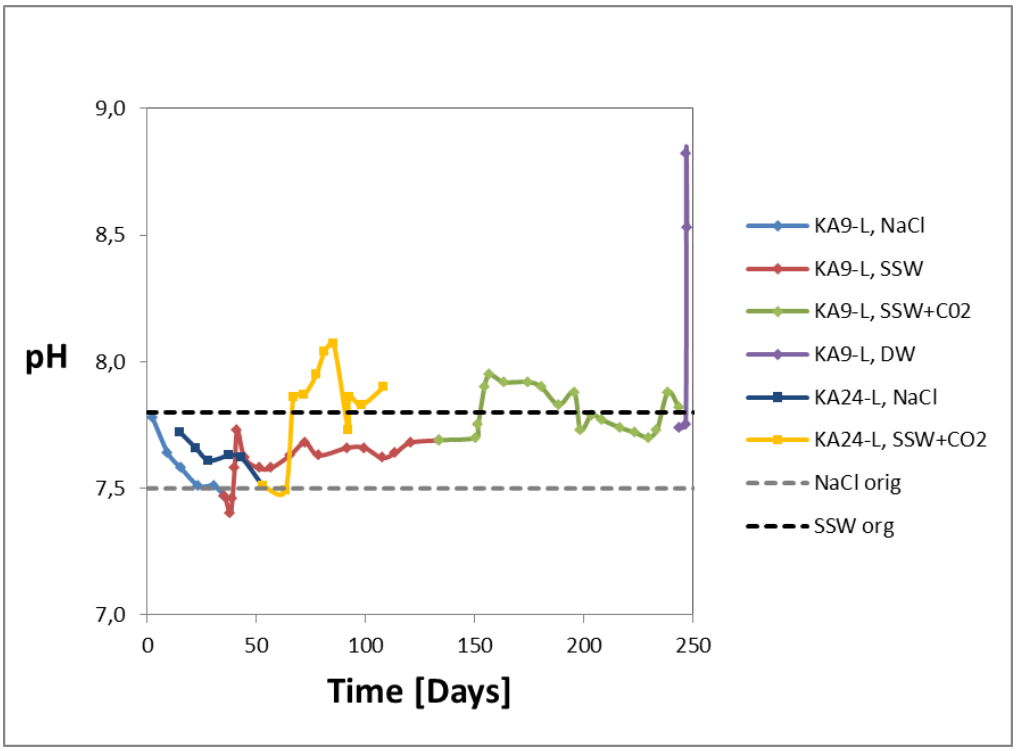

Figure 4-30: pH versus time for KA9-L and KA24-L.

5. DISCUSSION

Three long-term flooding experiments performed on Kansas chalk have been analyzed in this thesis, with the main objective of answering the questions: Does the injection of sea water reduce the mechanical strength of compacted outcrop chalk at elevated stress and temperature? And to what degree will the injection of carbonated sea water further contribute to reduce the mechanical strength? These questions will be evaluated through the following discussion.

5.1. Yield Analysis

The mechanical strength of the chalk cores can be determined based on several parameters such as the elastic modulus and the stresses at which irreversible deformation occurs, termed the yield point. A low yield point is associated with lower strength. The three cores were drilled from the same block such that the mechanical parameters could be compared. Mechanical properties like the yield point are affected by both the applied stress level, when considering for example the differential axial stresses, and the flooding fluid. The stress-strain relationships for KA9-L, KA24-L and KA28-U are shown in Figure 4-1, Figure 4-2 and Figure 4-3, respectively. The KA28-U core has the lowest yield point of 11.0 MPa. The yield analysis was performed by constant overburden stress of 42.7 MPa during pore pressure depletion from 38.0 to 15.0 MPa. The onset of yield is 14.5 MPa in KA9-L and 15.2 MPa in KA24-L tests. These tests were performed at constant pore pressure and increasing overburden stress by ramping of the piston pressure during uni-axial strain conditions such that that the side stresses are adjusted to ensure zero radial strain. The side stress adjustment affected the overburden stress according to Eq. 2-10. We observe that for the KA28-U-test the onset of yield occurred at lower value than the other tests. We can understand the discrepancy by introducing the effective stress relation and the

Biot stress coefficient α. The effective stress at yield is given by the overburden stress minus a fraction α of the pressure. In terms of the differential stresses this is expressed as,

$$\sigma_y{}' = \sigma_{OB,y} - \alpha P_{P,y} = \sigma_{OB,y} - \alpha(\sigma_{OB,y} - \sigma_y)$$

Nermoen, Korsnes et al. (2013) presented several ways of experimentally determining the Biot stress coefficient showing that for this exact block of chalk the Biot stress coefficient is around 0.9. This increases the yield value,

$$\sigma_y{}' = 42.7 - 0.9(42.7 - 11.0)MPa = 14.2\ MPa$$

In the other two tests which were performed at 0.7 MPa pore pressure the correction factor has less impact on the mechanical stress level.

Even though all cores are flooded with 1.11M NaCl during yield analysis, KA28-U is exposed to a higher stress level due to the Biot stress coefficient that reduce the effect of the pore pressure during depletion on the effective stress estimate. It is therefore reasonable that KA28-U has the lowest yield value.

E-modulus tells us something about the ability of the material to resist deformation where a high value is associated with lower resistance. According to Table 4-3 E-modulus is highest for KA28-U with a value of 2.8 KPa, while 2.3 for KA9-L and 2.2 for KA24-L.

As we can see from the stress-strain curves the transition from the initial elastic linear phase towards the fully plastic phase occurs over a range of stresses. There may be several underlying mechanisms that may cause such an observation. If the material is heterogeneous by nature the different parts of the plug may deform differently and have a range of yield values associated with it. In order to capture the average stress in which the plug starts yielding the pragmatic yield may be used. We can see how the stress-strain curves bend, especially in Fig. 4-1.

When estimating the yield values there are some freedom in how the yield is defined and which parameters that are used in the analysis. The estimate of the onset of yield depends on our choice of threshold value between the extrapolated linear trend and the observed deformation in the stress-strain curve. Typically if we chose a higher threshold value for the residue stress this leads to an increased onset of yield. In addition it is also up to the person who analyzes the test to define the limits in which a linear trend is observed. This applies to both the elastic and linear plastic phase. The strain at which the linear trends meet defines the pragmatic yield strain. At this time we can read off the stress state the plug is exposed to which defines the pragmatic yield. In this analysis we have employed the exact same rules such that the yield values can be compared for the different tests.

In addition, since it takes time to re-organize the grains and accommodate the deformation the rate of stress buildup affects the mechanical parameters.

5.2. q-p' Diagrams

q-p' diagrams in Figure 4-14, Figure 4-15 and Figure 4-16 are made to illustrate how the a re-pressurization phase and a depletion phase affect the chalk material. During depletion phase (i.e. increase in overburden stress (KA9-L and KA24-L) or reduction in the pore pressure (KA28-U) the core moves out from the elastic phase and in to the plastic phase were deformation is irreversible. We can see from Figure 4-14 how the core in KA9-L moves back again past the pragmatic yield and onset of yield values after re-pressurization. We are back within the end cape. This is because the mechanical stress applied in axial direction is lowered during re-pressurization phase. During yield phase, the pore pressure in KA28-U is reduced from 38Mpa to 15MPa. This increases the differential axial stress according to Eq. 2-

11. This is what actually happens in the reservoir when oil and gas are extracted. The pore pressure is reduced while the overburden stress from the overlying layers continues to press down on the reservoir rock with the same weight. Deformation is therefore expected to increase. The q-p' diagram for KA28-U is illustrated in Figure 4-16.

5.3. Creep Analysis

The axial creep strain as a function of time is plotted in Figure 4-4, Figure 4-5 and Figure 4-6 to show how the cores deform over time. Considering KA9-L, we do not observe any noticeable increase in strain rate when shifting from NaCl to SSW. In the study by Haddadi (2013) on Kansas chalk at 130°C , the change from NaCl to SSW showed no significant raise in creep strain.

The creep strain obtained after flooding with different fluids is given in Table 4-5. We can see that the axial creep strain has only increased from 3.9 % to 4.2 % at the end of SSW flooding in KA9-L. The outcome is quite different in KA28-U, where a distinct accelerating creep is observed when shifting from NaCl to SSW. The axial creep strain has increased from 5.5 % at the end of NaCl flooding to 9.0 % at the end of SSW flooding. We can see from Figure 4-7 how the strain rate is higher in the beginning and then decreases over time. The only remarkable exceptions are the one already mentioned when we change from NaCl to SSW flooding in KA28-U, and also when KA28-U is flooded with DW at the end of the test the axial strain is increased with 0.6%.

Table 4-5 show that the addition of 3 g/l CO_2 in the sea water has little effect to the observed axial strain. The axial creep strain only increase with 0.1, 0.4 and 0.2

% in KA9-L, KA24-L and KA28-U, respectively after adding CO_2 to the sea water. The increase is highest in KA24-L, but the core has not been flooded with SSW in advance. Most of the additional strain is probably due to the SSW and not the CO_2.

After two weeks with a concentration of 3 g/l CO_2, the concentration was increased to 10 g/l in KA28-U and continued for 35 days before increasing the CO_2 concentration additionally to 30 g/l. The increase to 10 mg/l had small effect on the axial creep strain that only had increased with 0.3 % at the end of the flooding period. After increasing the CO_2 concentration to 30 g/l and flooding for 31 days, no additional axial strain was observed. This tells us that after flooding the KA28-U core with carbonated water for 80 days in total, the axial creep strain has increased with only 0.5 %.

To evaluate how changes in pore fluid composition alter creep curves, we tried to find a suitable statistical parameterization that could fit the different experimental flooding stages in our tests. Power-law was chosen after considering different models. The tests presented are long-term experiments with thousands of measurements. Using a statistical parameterization as power-law enables us to condense these thousands of measurements into a model of only two parameters.

Power-law is a monotonous increasing function with a steadily decaying rate when $B<1$ and $A>0$. The values for A and B used in our tests are presented in Table 4-4. All values of B is less than 1 and all values of A is greater than 0, and power-law mimics the axial creep strain where the rate is reduced through time and is larger than zero. We can observe an abrupt accelerating creep in KA28-U from Figure 4-6 when changing from NaCl to sea water. At accelerating creep, the strain rate is increasing and power-law does not fit this stage to a satisfying degree. A square-time dependency (see chapter 2.6.4) was implemented with the value of A set to $3.9 \cdot 10^{-6}$.

There are no effluent samples to analyses chemically because of the varying pore pressure in the KA28, and it is not possible to investigate if the concentration of any ions has changed. But from evaluating and compare findings in other research with our one result, we can suggest a possible reason for the accelerating creep observed.

Geitle (2013) and Abubeker (2013) also experienced an accelerating creep after changing the flooding fluid from NaCl to SSW. From the chemical analysis of the effluent, they found that the concentration of magnesium ions in the effluent decreased and the concentration of calcium ions increased. At the same time, the concentration of sulfate ions in the effluent was lower than the original concentration of the flooding fluid, indicating precipitation of anhydrite (See Eq. 2.7). The loss of calcium ions induces dissolution when the equilibrium is altered. The test failed a few days later because of clogging.

Megawati, Hiorth et al. (2013) performed a comprehensive stud entitled *"The Impact of Surface Charge on the Mechanical Behavior of High Porosity Chalk"*. They conclude that when flooding with a fluid containing sulfate at 130°C, sulfate is adsorbed to the positively charged chalk surface. The surface becomes negatively charged through the adsorption of sulfate, repulsive forces will arise close to the granular contacts which in turn will weaken the material even further by pore collapse resulting from the local shear failure between grains. They relate sulfate adsorption to pH, where the adsorption decreases with increasing pH. Based on analytical calculations, they report that the adsorption at pH below 4 is constantly large. But they emphasize that it should be further investigated. The adsorption of sulfate is also temperature dependent and will be affected by the concentration of sulfate. The influence of sulfate is greater when these two parameters are increased, and they report of a sulfate adsorption two times higher at 130 °C than at 50 °C. So one possible

explanation to the accelerating creep seen in Figure 4-6 is that altering the brine composition from NaCl to SSW causes a change in surface potential by the adsorption of sulfate presented in the SSW. We have used a square time dependency in order to fit the stage of accelerating creep. After five days the accelerating creep stops. This can possibly be linked to the time it takes to fill all available surface sites with sulfate. The creep curve continues to increase after this point, but with a continuously reducing rate as before the accelerating creep was initiated. The addition of CO_2 in the SSW will increase the acidity according to Eq. 2-2 and dissolve calcite. New reactive surface will be generated through the combination of dissolution and reduction in pore volume by grain crushing and re-arrangement. Even though the axial creep strain continuous to increase after the addition of CO_2, the creep curve is not that steep and the rate is lower than when only flooding with sea water. It can be interpreted as if the dissolution of calcite that would be expected from the acidification is quite small. And the addition of CO_2 does not seem to have any significant impact on the compaction of the chalk core. These findings contradicts the result of Korsnes, Madland et al. (2008) where flooding with carbonated water increased the strain rate per pore volume significantly by a factor of 2.5 compared to flooding without non-carbonated SSW. We know that there are several factors that affect the mechanical properties of the chalk. The solubility of $CaCO_{3(s)}$ decreases with increasing temperature. The tests by Korsnes, Madland et al. (2008) are performed at ambient temperature. While the long-term experiments presented here have a temperature of 90°C in KA9-L and KA24-L and 130°C in KA28-U. Thus, it is reasonable that the dissolution is more pronounced at ambient temperature. The strength will also vary between different chalk types. Kansas chalk seems to be a strong type of chalk.

5.3.1. PRESSURE DEVELOPMENT THROUGH TIME

Figure 4-8, Figure 4-9 and Figure 4-10 are plotted to illustrate how the different stresses evolve over time and how they are related to each other.

For uniaxial strain conditions, the radial stress needed is related to the mechanical strength at a given overburden. We can see especially from Figure 4-8 how the confining pressure in radial direction is adjusted when the piston pressure in axial direction changes. To always maintain uniaxial strain which entails strain in only axial direction, the confining pressure is increased when the piston pressure decrease. And conversely, when the piston pressure is increasing, the confining pressure decreases.

From Figure 4-8 we can see how the axial differential stress is changed at re-pressurization phase for KA9-L. The axial differential stress is reduced from 27 to 11 MPa and is constant through the rest of the test. For KA24-L and KA28-U the axial differential stress is constant at 27 MPa and 27.7 MPa through the creep phase. All tests are performed with a constant pore pressure during creep phase according to Figure 4-8, Figure 4-9 and Figure 4-10. The pore pressure is 0.7 MPa in KA9-L and KA24-L, while the pore pressure is much higher in KA28-U with a value of 15 MPa.

There are two remarkable pressure changes in Figure 4-8 for KA9-L. After 156 creep days we can observe a fall in the confining pressure, piston pressure and axial differential stress. This is cause by the Quizix pump that failed. After 180 creep days the pump configuration had to be fixed and can explaine the observed increase in confining pressure and the decrease in piston pressure.

In Figure 4-10 for KA28-U we can see that there are some variations after approximately 150 creep days. There were some problems with the test during the

weekend because the Isco receiving pump was full, causing an increase in pore pressure and an increase in axial differential stress. The receiving pump has to be emptied and the stress levels were adjusted.

In Figure 4-9 for the KA24 test we observe how the confining pressure had to increase when carbonated sea water was introduced to the plug. This comes from the automatic regulation performed by Labview which indicate a weakening of the plug when sea water is introduced.

5.3.2. PERMEABILITY DEVELOPMENT

The permeability and differential pressure has been plotted as a function of time in Figure 4-11, Figure 4-12 and Figure 4-13. The variations in permeability are high. Haddadi (2013) observed how the permeability decreased when the creep strain was increased in two cores from Kansas chalk flooded with NaCl and SSW. This trend is not that noticeable in the three tests presented here. The permeability, which can be expressed through Darcy's law (see chapter 2.6.5) is influenced by several factors. The rate is one of them, but the rate in the three experiments is 0.01 ml/min in the creep phase. Differential pressure however is unstable and we can observe large fluctuations which affect the permeability. When flooding with carbonated sea water, the varying differential pressure can be related to $CO_{2(g)}$. If some of the carbon oxide occur as gas and not as dissolved $CO_{2(l)}$ in sea water, gas bubbles may escape through the flexible membrane in the back pressure regulator and thereby reduce the pressure on the down flooding side. The differential pressure will increase and consequently the permeability is reduced.

In order to observe any potential gas bubbles we changed some of the tubing in the KA9-L test to plastic tubing. We could clearly see zones with fluid followed by gas bubbles. We also changed the flooding fluid back to non-carbonated sea water for a short time to check if the differential pressure would stabilize. The differential pressure dropped to around 25-30 Mpa with still some flocculation. But the fact that the differential pressure deceased so fast after changing to non-carbonated sea water are a clear indication of the two phase effects present when flooding with carbonated sea water. Gas bubbles may escape through the flexible membrane in the back pressure regulator and thereby reducing the pressure on the down flood side. The differential pressure will increase and consequently the permeability is reduced.

5.3.3. POROSITY EVOLUTION

The porosity will be altered as the core compacts. The porosity is a measure of the pore space in a material. When the pore space collapse, it is reasonable that the porosity will decrease. We name this porosity mechanical porosity. But pore collapse is not the only mechanism taking place within the core. Flooding with a fluid not in equilibrium with the core can cause mineral dissolution. When the strain rate decreases over time and material dissolves, we expect a bigger difference between total porosity (mechanical and chemical contribution) and mechanical porosity. In Figure 4-17 and Figure 4-18 $\phi_{(mech)}$ and $\phi_{(mech+chem)}$ are calculated according to Eq. 2-40 and Eq. 2-42 respectively. The total porosity includes the change in solid volume. As mentioned in chapter 4.1.5, we have included a correction of the mass and we assume that the change in density develops linearly. Obviously, this is not an ideal way of doing it. But the correction and assumption are made in order to show the idea behind how both pore collapse and dissolution affect the porosity. The gap between

total porosity and mechanical porosity is the chemical contribution from dissolution inside the core, seen as the yellow line in Figure 4-17 and Figure 4-18.

$\phi_{(mech+chem)}$ is 37.0 % in the beginning of the creep phase and 35.0 % at the end of the test in KA29-L. For KA24-L $\phi_{(mech+chem)}$ is 33.7 % in the start of the creep phase and decreases to 31.4 % after test. In both tests, $\phi_{(mech+chem)}$ is higher than $\phi_{(mech)}$ with a difference of approximately 1.8 % in KA9-L and approximately 0.2% in KA24-L at the end of the test. We interpret the difference as the chemical effect.

It is not surprising that the difference between $\phi_{(mech+chem)\ and}\ \phi_{(mech)}$ is larger in KA9-L since this test has been flooded for 249 days in total compare to 109 days for KA24-L. And the creep strain rate decreases over time, while the dissolution continues. The mass loss is 0.56 g and 0.46 g in KA9-L and KA24-L, respectively. Thus, the mass loss of KA9-L is just 0.16% more than that of KA24-L. But also two other parameters are different between the two tests. The density difference and the axial strain are also incorporated in Eq. 2-42. The change in density is bigger in KA9-L where ρ is increased with 0.03 g/ml. The density change in KA24-L is an increase of 0.01 g/ml. The last parameter effecting the calculation of $\phi_{(mech+chem),}$ the axial strain, is increased much faster in KA24-L than KA9-L because of no re-pressurization phase. We have mentioned several times that the stress level has an impact on the observed axial stress. The axial strain has reached 6% at the end of the KA24-L test (109 days) compared to 8% in KA9-L (249 days).

The next step in evaluating the porosity evolution through time is to compare the $\phi_{(mech+chem)}$ and $\phi_{(mech)}$ from Eq. 2-40 and Eq. 2-42 with the calculated porosity from Eq. 2-29 based on the before and after measurements of the core. To evaluate the match between the different porosity calculations in Table 5-1, the length at the

end of the test L_{end}, the change in density $\Delta\rho$, total porosity $\phi_{(mech+chem)}$ and mechanical porosity $\phi_{(mech)}$ are summarized in Table 5-2.

Test name	1 Measurements Before/after test			2 Measurements Labview/IC-data/pycnometer		
	$\phi_{(mech+chem)}$ %	$\phi_{(mech)}$ %	$\phi_{(chem)}$ %	$\phi_{(mech+chem)}$ %	$\phi_{(mech)}$ %	$\phi_{(chem)}$ %
KA9-L	33.91	32.91	1.00	35.05	33.27	1.78
KA24-L	32.27	32.63	-0.36	31.36	31.12	0.24
KA28-U	32.15	30.67	1.48	-	30.02	-

Table 5-1: Porosity calculations based on before and after measurements of the plug and from Labview, IC and pycnometer measurements

Test name	1 Measurements Before/after test			2 Measurements Labview/IC-data/pycnometer		
	L_{end} mm	$\Delta\rho$	ε_A %	L_{end} mm	$\Delta\rho$	ε_A %
KA9-L	64.62	0.02	8.54	64.88	0.03	8.04
KA24-L	70.97	-0.03	4.25	69.72	0.01	6.34
KA28-U	65.36	0.04	12.04	64.42	-0.01	12.87

Table 5-2: Parameters included in porosity calculations based on before and after measurements of the plug and from Labview, IC and pycnometer measurements

For simplicity, we call them Meas.1 and Meas. 2 as seen from the tables above.

We only have the mechanical porosity for comparison in KA28-U. $\phi_{(mech)}$ in Meas.1 is 0.65% higher than $\phi_{(mech)}$ in Meas.2. Based on Meas.1, the difference between $\phi_{(mech+chem)}$ and $\phi_{(mech)}$ at the end of the test is 1.48%. Said in other words, the mechanical contribution to porosity based on Meas.1 for KA28-L is 1.48% at the end of the test.

In KA9-L, $\phi_{(mech+chem)}$ is higher than $\phi_{(mech)}$ based on both types of measurements. The difference between $\phi_{(mech+chem)}$ and $\phi_{(mech)}$ is 1 % in Meas. 1 and 1.78 % in Meas. 2.

In KA24-L $\phi_{(mech+chem)}$ is 0.36 % lower than $\phi_{(mech)}$ based Meas.1. and 0.24 % higher than $\phi_{(mech)}$ in Meas. 2. Ideally, it would not be any difference in the two types of measurement. But there are some possible explanations to the distinction.

First of all, we can see from Table 5-2 that the length measurement of the plug after testing does not correspond completely with the length at the end in Meas. 2. Some elastic rebound could be expected when the stress applied is removed, and the length is thus somewhat increased. There could also be some minor stretching of the triaxial cell caused by the confining oil pushing from the sides.

The calculations of density based on before and after measurements of the core are performed according to Eq. 2-33. The other method to calculate density is from the pycnometer results. The density in KA9-L is increased after test independent of the measurement method applied. We can see from Table 5-2 that the density of KA24-L has decreased with 0.03 g/ml in Meas.1 and increased with 0.01 g/ml in Meas.2. While for KA28-U, the density has increased with 0.04 g/ml in Meas.1 and decreased with 0.01 g/ml in Meas. 2. The standard deviations from pycnometer measurments are given in Table 4-7. The density may vary in different parts of the core. Figure 5-1 illustrates how one of the core pieces after cutting is weaker at the edge than in the center.

Figure 5-1: Broken KA9-L core piece from the inlet side.

There is also a chance that the core has not been completely dried when the mass was measured on the scale, which will have an impact on the density calculations in Meas.1.

Also the axial strain is incorporated in Eq. 2.42 for estimating total porosity. We can see from Table 5-2 that there are also some small variations in the axial strains applied in the two different measurement methods.

The variations in several of the parameters incorporated in the porosity equations are not that large alone. But small variations in several parameters are significant in total, and accuracy during experimental performance is important.

5.3.4. STRAIN PARTITIONING

The observed axial strain depends on the mechanical stress level and the chemical induced strain arising from rock-fluid interactions. *Strain partitioning* simply means that we divide the observed strain into a mechanical part and a chemical part, which we have done for KA9-L and KA24-L in Figure 4-20 and Figure 4-21. $\varepsilon_{(chem)}$ is estimated from Eq. 2-45 and as already explained for the porosity calculations, we decided to use a mass correction and to assume a linear change in density to show the idea behind strain partitioning. KA9-L contains a re-pressurization phase. The differential axial stress of the core at pragmatic yield and onset of yield is 14.5 and 17.4 MPa. By re-pressurizing from 27 MPa to 11 MPa axial differential stress, we are within the area where the core behaves elastic. It can be explained as if the mechanical component is switched off, and the chemical component is the only contribute to the observed strain when we are flooding with a fluid affecting the equilibrium inside the core. Thus, the additional strain after re-pressurization phase is caused by mineral dissolution.

Before re-pressurization phase, the chemical component is switched off. We are flooding with an intact fluid of NaCl, and it is just the mechanical stress that causes the compaction. Therefore, $\varepsilon_{(mech+chem)}$ and $\varepsilon_{(mech)}$ coincides in Figure 4-20 and the chemical contribution is zero. In the same figure, $\varepsilon_{(mech+chem)}$ is increasing after re-pressurization, from the increase in $\varepsilon_{(chem)}$.

The difference between $\varepsilon_{(mech+chem)}$ and $\varepsilon_{(mech)}$ from Figure 4-21 is less in KA24-L than in KA29-L. No re-pressurization phase is carried out and the mechanical contribution to the axial strain continues to increase, but with a slower rate. As the dissolution continuous, the chemical contribution of the total axial strain

becomes more significant. At the end of the test, the chemical strain in KA24-L is 0.24 % and 0.53% in KA9-L.

It should also be noted that there might be cross terms involved. The possibility of if the imposed mechanical stress can induce chemical changes, should be investigated through further research

5.4. Chemical Analysis

According to Figure 4-22 there are no significant variations between the concentration of Cl^- and Na^+ ions in the effluent and the original concentrations of the standards in KA9-L. NaCl is inert with the chalk material.

From Figure 4-24 the concentration of Mg^{2+} is lower than the standard concentration while flooding with sea water. We do not observe an apparent increment in the Ca^{2+} concentration simultaneously. If we did, it could be an indication of ion substitution between calcium- and magnesium ions. Any specific change in sulfate concentration is neither observed when flooding with SSW. If the concentration of SO_4^{2-} dropped while the concentration of Ca^{2+} was below the original concentration of the standard, it would be an indication of precipitating $CaSO_{4(s)}$. The Mg^{2+} concentration increases above the standard concentration after initiating flooding with carbonated sea water. It can be interpreted as if magnesium ions are washed out from the core.

From Figure 4-26 the accumulated mass is -0.43 g at the end of the KA9-L test. It means that the weight of the core is reduced with 0.43 g. The correct weight loss from measuring the dry weight of the plug before and after testing is -0.56 g.

Figure 4-28 illustrates the charge balance of the effluent. The charge balance is satisfying since the cations and anions cancel each other out and the total charge balance is zero.

From Figure 4-23 and Figure 4-25 we can clearly see how all concentrations of ions are lower than the original concentrations of the standards through the KA24-L test. Calcium and bicarbonate ions are the only ions slightly above the concentration

of the standard. It is not just one ion increasing or decreasing at the time, but all ions at once. The shape of the curves for each ion represented is quite similar. If this is correct, the mass of the plug is 4.8 g higher after test from Figure 4-27. And Na^+ and Cl^- contribute with approximately 2 g each to the mass increment, which we consider as unlikely. Based on dry weight measurements of the plug, KA24-L has become 0.47g lighter during flooding.

The total charge balance in Figure 4-29 is close to zero when flooding NaCl, but deviates from zero after as we continue the test with carbonated water flooding.

The ionic chromatography test results for KA24-L can clearly not be trusted. But they are still presented to shed light upon possible errors and problems.

The repeatability of the standards in KA24-L was not satisfying, and we can see from the curves that flocculation in ion concentrations are systematically taking place in all ions at the same time. It should also be mentioned that there have been reported of problems with the ionic chromatography machine lately.

For KA9-L the deviations are not that clear. The difference between mass loss calculated from the ionic chromatography results and the mass loss from measuring the dry weight of the core before and after test is 0.13g. Especially the effluent samples from KA9-L have been stored for a many days, and even months before the chemical analysis was conducted. Even though the samples have been stored in the fridge, the possibility of evaporation could be present. The tops of the sample glasses may not be completely close. Some ions may have precipitated as minerals when standing still for a long time. If so, these ions will not be measured in the machine and the concentration of an ion will be lower than what is correct. Most of the effluent samples from KA9-L had a blur yellow color with some turbidity. This can be seen

from Figure 5-2. Rust residue could be observed at the bottom of the sample glass and also directly on the core (see Figure 5-4). If some minerals did precipitate in the effluent water, we would expect it to be white based on the ions present. But because of the corrosion products in the water, the color may be more yellow than white.

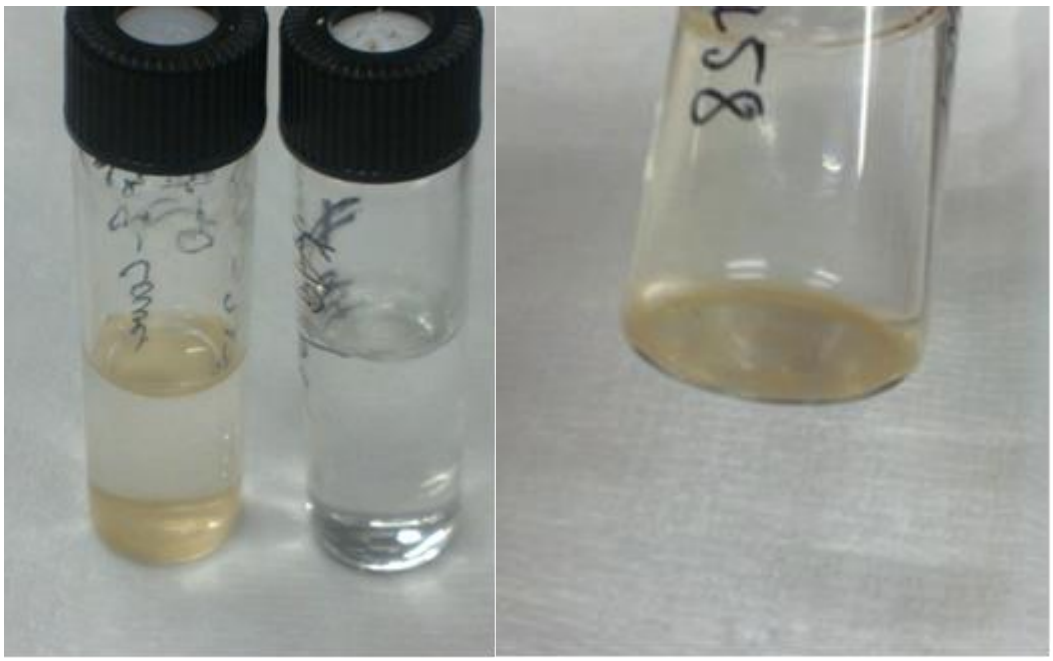

Figure 5-2: Effluent sample with a slightly yellow color and some precipitate compared to the clear sample.

Systematic errors in the ionic chromatography machine and in measurements are also always present.

pH measurements of the effluents are presented in Figure 4-30. From Eq. 2-2 we would expect a lower pH when CO_2 is dissolved in sea water. But we do not observe that from our pH measurement from KA9-L and KA24.L. Contrary, the alkalinity of the effluent increases when we are flooding with carbonated sea water. Not continuously, but in some parts of the curve in Figure 4-30. We consider two

possible explanations. First, these effluent samples have been stored for a long time as already mentioned. If they are not completely closed, it is reasonable that $CO_{2(g)}$ can escape. The test glasses have also been standing without the top on during preparation for the ionic chromatography and while measuring the pH. We need to conduct the pH measurements after the chemical analysis because the samples are contaminated from the pH-meter. It would give us a fare more useful measurement of the pH if we could implement it right after the effluent sample is removed from the flooding device. Secondly, why is the pH even sometimes higher than the pH of the flooding fluid SSW? We do not know what compounds there might be in the samples at this point. But we can observe some red/brown precipitate that we believe is some sort of rust from the equipment, and a slightly yellow turbid color of the effluent. Chemical reactions that we are not aware of could possibly explain the rise in pH.

6. CONCLUSION

Our analysis of three long-term experiments performed on Kansas chalk under uni-axial strain conditions has focused on how the dynamic evolution of the creep curve depends upon pore fluid composition and stress conditions. In addition, chemical analysis of the produced effluent water has been analyzed and integrated into the mechanical observations.

We do not observe an increase in the creep strain rate in any of the three experiments when flooding with carbonated water is initiated. The axial creep strain after flooding with carbonated water had only increase with 0.1, 0.4 and 0.5 %. Based on our findings we propose the conclusion that: Under in-situ conditions CO_2 dissolved in sea water does not increase the creep strain rate, but provides a small chemical driven additional strain eroding the volumes of the solids.

From our results, we can conclude that Kansas chalk is relatively strong compared to other chalk types with high elastic modulus and yield values. Similar research at realistic reservoir conditions should be performed with different chalk types to further investigate the long-term effects of CO_2 injection and the possibility of safe sequestration in carbonate reservoirs.

7. REFERENCES

"Calculation of thermodynamic state variables of carbon dioxide." from (http://www.peacesoftware.de/einigewerte/co2_e.html).

(1996, 01.01.2013). "Lov om petroleumsvirksomhet [petroleumsloven]." Retrieved 05.01.14, from http://lovdata.no/dokument/NL/lov/1996-11-29-72#KAPITTEL_4.

(2008). "Norwegian Storage Experience ". Retrieved 02.02.14, from http://www.regjeringen.no/upload/OED/Vedlegg/2008-05-22%20Lagring%20av%20CO2.pdf#search=co2

(2010). "Carbon Dioxide Enhanced Oil Recovery." Retrieved 14.11.13, from http://www.netl.doe.gov/technologies/oil-gas/publications/EP/small_CO2_eor_primer.pdf.

(2011). "CO2 storage atlas, Norwegian North Sea." from http://www.npd.no/Global/Norsk/3-Publikasjoner/Rapporter/PDF/CO2-ATLAS-lav.pdf.

(2012, 11.04.2012). "The petroleum sector - Norway's largest industry." Retrieved 14.11.13, from http://www.npd.no/en/Publications/Facts/Facts-2013/Chapter-3/.

(2013). "Carbonate Reservoirs." Retrieved 13.11.13, from http://www.slb.com/services/technical_challenges/carbonates.aspx.

Abubeker, E. A. (2013). Water weakening of chalks: comparison of intact and fractured cores. Stavanger, Universitetet i Stavanger. **Master**.
Masteroppgave i Petroleumsteknologi, Universitetet i Stavanger

Ahmed, A. N. (2013). "En eksperimentell studie av CO2 injeksjon for økt oljeutvinning i oppsprukket kalk."

Alam, M. M. (2011). "Rock physical aspects of CO injection in chalk 2."

Arts, R., et al. (2004). "Monitoring of CO< sub> 2</sub> injected at Sleipner using time-lapse seismic data." Energy **29**(9): 1383-1392.

Bachu, S. (2000). "Sequestration of CO2 in geological media: criteria and approach for site selection in response to climate change." Energy conversion and Management **41**(9): 953-970.

Bachu, S. (2008). "CO2 storage in geological media: Role, means, status and barriers to deployment." Progress in Energy and Combustion Science **34**(2): 254-273.

Benson, S. M. and D. R. Cole (2008). "CO2 sequestration in deep sedimentary formations." Elements **4**(5): 325-331.

Christensen, J. R., et al. (2001). "Review of WAG field experience." SPE Reservoir Evaluation & Engineering **4**(02): 97-106.

Delage, P., et al. (1996). Subsidence And Capillary Effects In Chalks, International Society for Rock Mechanics.

Emberley, S., et al. (2005). "Monitoring of fluid–rock interaction and CO< sub> 2</sub> storage through produced fluid sampling at the Weyburn CO< sub> 2</sub>-injection enhanced oil recovery site, Saskatchewan, Canada." Applied Geochemistry **20**(6): 1131-1157.

Emberley, S., et al. (2005). "Monitoring of fluid–rock interaction and CO2 storage through produced fluid sampling at the Weyburn CO2-injection enhanced oil recovery site, Saskatchewan, Canada." Applied Geochemistry **20**(6): 1131-1157.

Fjær, E., R., et al. (2008). Petroleum
Related Rock Mechanics (2nd Edition), Elsevier.

Gaus, I., et al. (2008). "Geochemical and solute transport modelling for CO< sub> 2</sub> storage, what to expect from it?" International Journal of Greenhouse Gas Control **2**(4): 605-625.

Geitle, K. (2013). Chemically induced compaction in fractured and intact chalk cores. Stavanger, Universitetet i Stavanger. **Master**.
Masteroppgave i Petroleumsteknologi, Universitetet i Stavanger

Gozalpour, F., et al. (2005). "CO2 EOR and storage in oil reservoir." Oil & Gas Science and Technology **60**(3): 537-546.

Grgic, D. (2011). "Influence of CO_2 on the long-term chemomechanical behavior of an oolitic limestone." Journal of Geophysical Research **116**(B07201): 22.

Gunter, W. D., et al. (2004). The role of hydrogeological and geochemical trapping in sedimentary basins for secure geological storage of carbon dioxide. **233:** 129-145.

Haddadi, D. (2013). An investigation of permeability and porosity evolution of Kansas chalk under in-situ conditions. Stavanger, Universitetet i Stavanger. **Master**.
Masteroppgave i Teknisk miljøvern, Universitetet i Stavanger

Hadizadeh, J. and R. D. Law (1991). "Water-weakening of sandstone and quartzite deformed at various stress and strain rates." International Journal of Rock Mechanics and Mining Sciences and **28**(5): 431-439.

Kaufmann, G. and W. Dreybrodt (2007). "Calcite dissolution kinetics in the system CaCO< sub> 3</sub>–H< sub> 2</sub> O–CO< sub> 2</sub> at high undersaturation." Geochimica et Cosmochimica Acta **71**(6): 1398-1410.

Korsnes, R., et al. (2006). "Impact of brine composition on the mechanical strength of chalk at high temperature." Eurock 2006b, Multiphysics Coupling and Long Term Behaviour in Rock Mechanics: 133-140.

Korsnes, R., et al. (2008). Enhanced chemical weakening of chalk due to injection of CO2 enriched water. International Symposium of the Society of Core Analysts, Abu Dhabi, United Arab Emirates.

Korsnes, R., et al. (2008). "Does the chemical interaction between seawater and chalk affect the mechanical properties of chalk." Eurock 2006a, Multiphysics Coupling and Long Term Behaviour in Rock Mechanics: 427-434.

Korsnes, R. I. (2007). Chemical induced water weakening of chalk by fluid-rock interactions. A mechanistic study, Universitetet i Stavanger. **PhD**.

Korsnes, R. I., et al. (2008). Enhanced chemical weakening of chalk due to injection of CO_2 enriched water. The International Symposium of the Society of Core Analysts Abu Dhabi.

Kvinge, G.-A. D. (2012). "En eksperimentell studie av CO2 lagring i sandstein og kalkstein med bruk av ulike avbildningsteknikker."

Le Guen, Y., et al. (2007). "Enhanced deformation of limstone and sandstone in precence of high P_{CO2} fluids." Journal of Geophysical Research **112**(B05421).

Liteanu, E., et al. (2013). "The influence of water and supercritical CO< sub> 2</sub> on the failure behavior of chalk." Tectonophysics **599**: 157-169.

Liteanu, E. and C. J. Spiers (2009). "Influence of pore fluid salt content on compaction creep of calcite aggregates in the presence of supercritical CO2." Chemical geology **265**(1–2): 134-147.

Madland, M., et al. (2011). "Chemical alterations induced by rock–fluid interactions when injecting brines in high porosity chalks." Transport in porous media **87**(3): 679-702.

Madland, M., et al. (2008). The effect of temperature and brine composition on the mechanical strength of kansas chalk. International Symposium SCA.

Madland, M., et al. (2009). Rock Fluid Interactions in Chalk with MgCl2 and Na2CI4 Brines with Equal Ionic Strength. 15th European Symposium on Improved Oil Recovery.

Madland, M. V. (2005). Water weakening of chalk: a mechanistic study. [Stavanger], UiS.
Avhandling (dr.ing./ph.d.) - Universitetet i Stavanger, 2005

Madland, M. V., et al. (2006). "The influence of CO2 gas and carbonate water on the mechanical stability of chalk." Journal of Petroleum Science and Engineering **51**(3-4): 149-168.

Martin, D. F., Taber, J.J., New Mexico Petroleum Recovery Research Center (1992). "Carbon Dioxide Flooding." Journal of Petroleum Technology **44**(4): 396-400.

Matthews, C. S. (1989). Chapter 6 Carbon Dioxide Flooding. Developments in Petroleum Science. G. V. C. Erle C. Donaldson and Y. Teh Fu, Elsevier. **Volume 17, Part B:** 129-156.

Megawati, M., et al. (2013). "The Impact of Surface Charge on the Mechanical Behavior of High-Porosity Chalk." Rock Mechanics and Rock Engineering **46**(5): 1073-1090.

Mungan, N. (1984). Carbon Dioxide Flooding — Fundamentals. Heavy Crude Oil Recovery. E. Okandan, Springer Netherlands. **76:** 131-176.

Mungan, N. (1991). An evaluation of carbon dioxide flooding. SPE western regional meeting, Society of Petroleum Engineers.

Nagel, N. (2001). "Compaction and subsidence issues within the petroleum industry: From Wilmington to Ekofisk and beyond." Physics and Chemistry of the Earth, Part A: Solid Earth and Geodesy **26**(1): 3-14.

Nermoen, A., et al. (2013). Measuring the Biot stress coefficient and its implications on the effective stress estimate US Rock Mechanics / Geomechanics Symposium. San Francisco, American Rock Mechanics Association

Norman J. Clark, H. M. S., W.P. Schultz, Kenneth Garms, and J.L. Moore, Core Laboratories Inc. (1958). "Miscible Drive - Its Theory and Application." Journal of Petroleum Technology **10**(6): 11-20.

Papamichos, E., et al. (1997). "An experimental and theoretical study of a partially saturated collapsible rock." Mechanics of Cohesive-frictional Materials **2**(3): 251-278.

Risnes, R. and O. Flaageng (1999). "Mechanical properties of chalk with emphasis on chalk-fluid interactions and micromechanical aspects." Oil & Gas Science and Technology **54**(6): 751-758.

Risnes, R., et al. (2003). "Chalk–fluid interactions with glycol and brines." Tectonophysics **370**(1): 213-226.

Risnes, R., et al. (2005). "Water weakening of chalk—Mechanical effects of water–glycol mixtures." Journal of Petroleum Science and Engineering **48**(1): 21-36.

Roehl, P. O. and P. W. Choquette (1985). Carbonate petroleum reservoirs.

Rutqvist, J., et al. (2010). "Coupled reservoir-geomechanical analysis of CO2 injection and ground deformations at In Salah, Algeria." International Journal of Greenhouse Gas Control **4**(2): 225-230.

Røgen, B. and I. L. Fabricius (2002). "Influence of clay and silica on permeability and capillary entry pressure of chalk reservoirs in the North Sea." Petroleum Geoscience **8**(3): 287-293.

Sulak, R. (1991). "Ekofisk field: the first 20 years." Journal of Petroleum Technology **43**(10): 1,265-261,271.

Sylte, J., et al. (1999). Water induced compaction in the Ekofisk Field. SPE annual technical conference.

Verdon, J., et al. (2013). A Comparison of Geomechanical Effects at Three'Megatonne'CO2 Storage Sites-Sleipner, Weyburn and In Salah. 75th EAGE Conference & Exhibition incorporating SPE EUROPEC 2013.

Vuillaume, J.-f. E., et al. (2011). CO2 injection Efficiency, Synthesis of Conceptual Chalk Model: Incremental Oil Recovery and CO2 Storage Potential. Brasil Offshore. Macaé, Brazil, Society of Petroleum Engineers.

Zangiabadi, B., et al. (2009). Chemical water weakening of various outcrop chalks at elevated temperature. Poromechanics IV: Proceedings of the 4th Biot Conference on Poromechanics.

Øvstebø, K. A. (2011). A mechanical study of the sulphate effect on chalk, Universitetet i Stavanger. **Master**.